MSUCL-186

A Survey of the (^{3}He,^{7}Be) Reaction at 70 MeV*

W.F. Steele, P.A. Smith, J.E. Finck
Cyclotron Laboratory, Michigan State University
East Lansing, Michigan 48824

and

G.M. Crawley

Physics Department and Cyclotron Laboratory
Michigan State University, East Lansing, Michigan 48824

and

Nuclear Physics Department
Australian National University, Canberra, Australia

ABSTRACT

A study of the (^{3}He,^{7}Be) reaction has been undertaken using a 70 MeV ^{3}He beam. By surveying a wide range of target nuclides, namely ^{12,13}C, ^{16}O, ^{24,26}Mg, ^{40,42,44}Ca, ^{58,60,62,64}Ni, ^{90}Zr, ^{120,124}Sn, ^{144}Sm and ^{206}Pb, systematics of the α-clustering phenomenon were investigated. In addition, masses and energy levels of ^{60}Fe and ^{120}Cd were measured. The ^{7}Be particles were detected in a single wire proportional counter backed by a plastic scintillator in the focal plane of an Enge spectrometer to ensure adequate particle identification. Total energy resolution as small as 140 keV full width at half maximum was obtained, although in most cases the target thickness limited the energy resolution to larger values. Differential cross-sections as low as 20 nb/sr were measured. The finite range programs LOLA[11] and LOLITA[11] were used to calculate differential cross-sections for comparison to data, assuming the reaction to proceed by a direct α-transfer. The spectroscopic factors which were extracted show a marked decrease with increasing atomic mass number, implying a decrease in surface alpha clustering for heavier nuclei.

NUCLEAR REACTIONS ^{12,13}C, ^{16}O, ^{24,26}Mg, ^{40,42,44}Ca, ^{58,60,62,64}Ni, ^{90}Zr, ^{120,124}Sn, ^{144}Sm, ^{206}Pb(^{3}He,^{7}Be), E = 70.0 MeV; measured σ(θ); deduced S_{α}'s.

* Work supported by the National Science Foundation.

1. Introduction

Various attempts have been made to measure the amount of α-clustering on the nuclear surface both by K^- meson capture experiments[1,2] and by $(\alpha, 2\alpha)$ reactions.[3] The results of these experiments are still inconclusive.

Another approach has been to look for α-cluster transfer reactions. If reactions which transfer two protons and two neutrons like $(^6Li,d)$ $(^7Li,t)$ $(d,^6Li)$ or $(^3He,^7Be)$ can be shown to proceed predominantly as the direct transfer of an α-cluster, then reaction calculations might allow the extraction of α-particle spectroscopic factors which may be taken as an indication of α-clustering. For example, Gutbrad, Yoshida and Bok,[4] and Martin, et al.[5] have extracted α-spectroscopic factors using the $(d,^6Li)$ reaction. However, the direct character of the $(d,^6Li)$ reaction is questionable. Comfort, et al.[6] conclude that multistep processes are important in $(d,^6Li)$ reactions probably at all energies. On the other hand, the $(^3He,^7Be)$ reaction seems more likely to proceed via direct α-pickup. Detraz, et al.[7] find that at 30 MeV incident ^3He energy, the reaction is probably predominantly direct. Further work by Detraz, et al.[8] shows that, for the most part, the α-particle is transferred in its ground state rather than in an isospin one excited state.

Target nuclides as heavy as ^{93}Nb[9,10] have been studied at ^3He energies as high as 40 MeV. The peak differential cross section is observed to sharply decline from ^{12}C to ^{40}Ca. However, the decrease is arrested past calcium. The ^{93}Nb data even implies

that the cross-section may rise for heavier targets. The present experiment extends previous work to heavier masses and higher bombarding energies. The higher ^3He beam energy of 70 MeV helps to assure a direct reaction mechanism, avoids the Coulomb barrier even for heavy nuclei and highly excited states, and raises the ^7Be ejectile energy, thus easing detection difficulties.

Finite range calculations using the codes LOLA[11] and LOLITA[11] were carried out for a number of transitions. Spectroscopic factors were also extracted.

In addition to nucear structure information, the $(^3He,^7Be)$ reaction presents the opportunity to study nuclides for which little information is available. In particular, the masses and some energy levels of ^{60}Fe, ^{120}Cd were measured in the present experiment.

2. Experiment

The experiment used the 70 MeV ^3He beam from the Michigan State University Cyclotron. The ^7Be particles were detected at the focal plane of an Enge split pole spectrograph using a single-wire proportional counter backed by a plastic scintillator. The experimental difficulties with this reaction include the small cross sections even at forward angles (less than 1 μb/st for heavy targets), the substantial kinematic broadening, and the large energy loss of the ^7Be ions, which requires the use of thin targets. The Enge spectrograph is therefore a very appropriate detector for this reaction. Since it allows the use of a reasonably large solid angle (1.2×10^{-3} steradian) as well as compensates

for kinematic broadening. Dispersion matching in the spectrograph also permits fairly large beam currents of up to 30 μ-ampere to be used without loss of resolution. The limitation on energy resolution in almost all cases is target thickness.

The yield of ^{3}He,α, t and ^{6}Li particles from the target is much greater than that of ^{7}Be. Furthermore the differential energy loss of $^{7}Li^{3+}$ ions crossing the focal plane at a given point is very nearly the same as that for $^{7}Be^{4+}$ ions at the same point. These facts present a severe challenge to the reliability and efficiency of a particle identification system. The detector arrangement is shown schematically in Fig. 1. The front detector, placed at the focal plane of the magnet is a single wire gas-filled proportional counter. Thin windows of Havar, Mylar or Kapton, 1 cm. high by 25 cm. long on either side of a slotted 1 cm. thick aluminum block contains a gas mixture consisting of Ne(85%), he(10%) and CO_2(5%). A nichrome wire 10 or 20 μm in diameter runs the length of the counter and is attached to external connectors at either end. Each end of the counter is fitted with a gas connection to allow a flow of gas through the counter, both to maintain the quality of the gas and to satisfy the requirements of a pressure regulation device.

Signals from each end of the counter are processed by charge sensitive preamplifiers and linear amplifiers. The sum signal and the signal from one end are both digitized and sent to the computer. The sum signal represents the total energy deposited in the counter; the second signal from one end of the counter represents the product of energy loss and the position of the event. The computer program TOOTSIE[12] accepts the digitized

signals then divides the second input by the first, yielding the position of the event. The results are plotted as a two dimensional array of energy loss versus position on a storage oscilloscope screen. Curves may be drawn on the screen to specify to the computer regions to be accepted.

Unfortunately, the energy resolution of the proportional counter is inadequate to provide band separation sufficient to assure reliable particle identification. Measurement of the ion time of flight in the spectrograph supplies the additional information needed for a satisfactory solution. A plastic scintillator attached by a light pipe to a photomultiplier tube (RCA 8575) is placed behind the proportional counter. The amplified signals from the anode of the phototube start a time to amplitude converter which is stopped by the cyclotron radio frequency signal. Since the time of flight of a charged particle in a magnetic field is inversely proportional to its charge to mass ratio, the time spectrum so obtained may be used to discriminate ions of different charge to mass ratios. Fortunately, no light ion other than $^{7}Be^{4+}$ has a charge to mass ratio of 4/7. Figure 2 shows a typical time of flight spectrum for a spectrometer entrance slit of 2^{o} x 2^{o}. The time resolution is clearly adequate to achieve excellent particle identification.

Target quality is another critical component of this experiment. Because of the relatively large differential energy loss of ^{7}Be ions, the targets must be thin, about 200 to 500 $\mu g/cm^2$ depending on the atomic number, for adequate resolution. Good energy resolution is especially important since each level of

the residual nucleus produces two peaks in the spectrum; the primary peak corresponding to the ground state and the secondary peak to the 429 keV first excited state of ^{7}Be. A small (about 100 keV) and normally negligible broadening of the secondary peak is caused by the decay of the ^{7}Be excited state. Furthermore, the differential cross-section for the (^{3}He,^{7}Be) reaction on ^{12}C and ^{16}O is significantly larger than that for other targets. Consequently, contamination of the targets by carbon and oxygen, a condition difficult to avoid especially for thin targets, must be minimized.

The targets are described in Table I. The magnesium, nickel, and zirconium targets were commercially obtained rolled foils. The oxygen target was prepared by vacuum evaporation of tungsten oxide onto a gold foil. The calcium targets were prepared by two methods. Both methods used the technique of reducing calcium oxide with zirconium powder in a heated zirconium tube. The liberated calcium metal was condensed onto either a 20 $\mu g/cm^2$ carbon foil, supported by formvar, or a loosely held 500 $\mu g/cm^2$ gold foil. Preparation, storage, and transfer of the targets were carried out in vacuum. The tin targets were prepared by reducing the oxide in a heated tantalum tube. The metallic tin was condensed onto a glass substrate coated with a thin film of CsI. The coating of tin was floated off in water to make a self-supporting foil in spite of the attempts to keep the targets free of carbon and oxygen, reaction products from these elements are obvious in most spectra.

3. Results

Because of the strength of contaminant peaks and the appearance of doublet peaks for each energy level of the residual nuclide, a computer program was used which was able to disentangle over-lapping peaks from one another as well as from a smooth background. The peak location together with the magnet calibration was used to calculate the excitation energy of the level in the residual nucleus. To determine the calibration, the excitation energies of known levels observed in the proportional counter were used to calibrate distance along the focal plane in terms of channel number. After corrections for energy loss in the target, the excitation energy of an unknown peak may then be computed. The results for the various targets are now presented.

3.1 ^{12}C(^{3}He,^{7}Be)^{8}Be

Levels observed in ^{8}Be are shown in Table II together with the peak cross-section obtained. Levels through 18.9 MeV of excitation energy were seen in this reaction but the peaks for the higher levels and the ground state may not be simultaneously placed on the counter. Therefore, measurement of spectra for the ^{12}C target was split into two parts, one each for the two ranges of excitation energy. Figure 3 displays spectra for the low lying and higher excitation energies. The resolution is limited by the target thickness to about 150 keV. The doublet structure for the ground state is clearly seen but the 2^{+} and 4^{+} level at 11.4 MeV shows up clearly and its cross-section increases relative to the ground state as the scattering angle increases.

Angular distributions for the states observed in ^{8}Be are shown in Figures 4,5. The solid line through the points is included for visual convenience and has no theoretical significance. Whenever possible, angular distributions corresponding to both the ground state and the first excited state of ^{7}Be are plotted. Since these two states in ^{7}Be have very similar wave functions, being just the $j=j=\pm 1/2$ pair in the 0p shell, then in a simple direct model of the reaction the cross-sections for these states would just be in the ratio of $(2j+1)$, that is the ground state cross-section would be exactly twice the excited state cross-section. For the ^{8}Be ground state case the ratio of secondary to primary peak cross-section is plotted in Fig. 4. The ratio varies smoothly from a value of close to 0.5 at forward angles through 0.8 near 30° and back to about 0.4 near 60° . The overall agreement in the shape of the two angular distributions suggests that the assumption of a direct transfer mechanism is reasonably accurate although the fact that the ratio of cross sections does change with angle implies some departure from this simple mechanism. The angular distributions for the other states are all rather flat except for the 2^{+} state at 2.90 MeV which shows some forward peaking.

Note also the excitation of the 1^{+} state at 17.64 MeV and either the 18.91 MeV (2^{-}) or 19.06 MeV (3^{+}) states. While these unnatural parity states are strictly forbidden in an α-transfer process, the fact that they are weakly excited again implies some, albeit small, departure from a simple direct transfer mechanism.

3.2 $^{13}C(^{3}He,^{7}Be)^{9}Be$

Two sharp levels in ^{9}Be, the $3/2^{-}$ ground state and $5/2^{-}$ state at 2.43 MeV, are observed as may be seen in Fig. 6. The 200 $\mu g/cm^{2}$ ^{13}C target limits the resolution which is nevertheless adequate for the primary and secondary peaks to be resolved. The broad level which could correspond to either the 2.78 MeV or 3.06 MeV levels is seen at a few forward angles, but is difficult to extract from the secondary peak of the 2.43 MeV state. No evidence for the 200 keV wide 1.68 MeV ($1/2^{+}$) level is discernable at any angle. Several broad levels also appear at angles greater than 30° centered around excitation energies of 4.8±0.2 MeV, 7.3±0.2 MeV and 11.9±0.4 MeV.

Angular distributions for the primary and secondary peaks for the ground and 2.43 MeV state are shown in Fig. 7. For both of these states the ratio of the cross-sections is almost constant with the value 0.5.

3.3 $^{16}O(^{3}He,^{7}Be)^{12}C$

Only the ground state and 4.44 MeV, 2^{+} state are strongly excited in this reaction as shown in Fig. 8. The 7.65 MeV 0^{+} and 9.64 MeV 3^{-} states appear only at a few angles. This weak excitation of the 3^{-} state is in marked contrast to the fairly large cross-section for this state observed in the $^{16}O(d,^{6}Li)^{12}C$ reaction.[6] Except for a group of weak unresolved levels around 13.35 MeV excitation energy, higher levels are not seen. The ratio of cross-sections for the ground state to 7.65 MeV state is about 4 : 1, compared to ratios of 8 : 1 found in the $(d,^{6}Li)$ reaction at 20 MeV[4] and about 6 : 1 in $(^{3}He,^{7}Be)$ at 30 MeV.[7]

Angular distributions for the ground and 4.4 MeV state are shown in Fig. 9. The ground state shows a strong forward peak, the cross-section decreasing by about a factor of 50 from 20° to 50°. However, the ratio of secondary to primary differential cross-sections are not close to 0.5 as was observed for the $^{13}C(^{3}He,^{7}Be)^{9}Be$ reaction.

3.4 $^{24}Mg(^{3}He,^{7}Be)^{20}Ne$

The spectrum shown in Fig. 10 indicates that four states in ^{20}Ne are strongly excited, the ground state, 1.63 MeV 2^+, 4.25 MeV 4^+ and 5.62 MeV 3^- states. In contrast with the small cross-section for the lowest 3^- in ^{12}C, the 5.62 MeV state is the strongest level observed. The unnatural parity 2^- state at 4.97 MeV has a peak cross-section only one quarter that of the 1.63 MeV 2^+ state but a fairly complete angular distribution is presented in Fig. 11.

At higher excitation energy the spectrum is partially obscured by contaminant peaks. Additionally the levels become close enough together that it is difficult to uniquely identify a peak in the spectrum with a particular level in ^{20}Ne. One can say however, that, as for $^{16}O(^{3}He,^{7}Be)^{12}C$, the first excited 0^+ state at 6.72 MeV is not strongly excited compared to the ground state. This is a peak observed at around 7.2 MeV which may include contributions from both the 7.17 MeV 3^- and 7.20 MeV 0^+ states. Other peaks are seen at 7.82 MeV (2^+) and 8.6 MeV.

The angular distributions, shown in Fig. 12 are generally much more structured than for the lighter nuclei. While there is a qualitative similarity in the shape of the angular distribution

of the primary and secondary peaks for the same final state, the ratio of secondary to primary cross-sections is not constant, except for the 1.63 MeV 2^+ state where the two distributions do differ by about a factor of 2.

In particular, for the ground state transition the cross-section for the secondadary ^{7}Be peak shows a pronounced dip near 13 degrees. This region was traced out in 1° steps with a 1° wide aperture. The ratio of the secondary to the primary peak was observed to fall to about 0.2. A similar effect, of the secondary peak showing more pronounced structure, was also observed by Detraz, et al.[7] for the $^{12}C(^{3}He,^{7}Be)$ reaction at 30 MeV.

3.5 $^{26}Mg(^{3}He,^{7}Be)^{22}Ne$

States observed in ^{22}Ne are shown in Table III and a spectrum is displayed in Fig. 13. The unnatural parity state at 5.14 MeV (2^-) is only very weakly excited. Above 5.5 MeV of excitation, it is difficult to identify peaks with known states because of the high level density. Even though the angular distributions for the two peaks at 5.57 MeV and 6.00 MeV are quite similar, in nearly all spectra the peak at 6.00 MeV is larger than the 5.57 MeV peak, so that an additional level is presumably excited around 6.00 MeV. The peak seen at 6.00 MeV must include the secondary peak of the 5.57 MeV state. A similar situation exists for the peaks at 6.42 and 6.85 MeV. Since the shapes of these cross-sections are very similar, it can be assumed that the secondary peak of the 6.00 MeV level makes a small contribution to the peak at 6.42 MeV. As for the case of ^{20}Ne, the strongest peak in the spectrum is at fairly high excitation energy, in this case a peak at 7.52 MeV.

Angular distributions for all the peaks observed are shown in Figs. 14 and 15. The ground state transition is quite similar to that for the $^{24}Mg(^{3}He,^{7}Be)^{20}Ne$ reaction. It exhibits a maximum around 22° and a minimum near 30 degrees. The remaining states with higher spin are less easily compared.

3.6 $^{40}Ca(^{3}He,^{7}Be)^{36}Ar$

A spectrum from $^{40}Ca(^{3}He,^{7}Be)^{36}Ar$ is shown in Fig. 16. The ground state, 1.97 MeV (2^+), and a group, which includes the 4.33 MeV (0^+), 4.41 MeV (2^+), and 4.44 MeV (4^+), are the strong groups. While the separate states that make up the third group cannot be resolved the energy calibration indicates that this group corresponds predominantly to the 4.44 MeV state. The 4.18 MeV (3^-) state is visible but weak. In addition a weak group which includes the 5.17 MeV (5^-) and 5.20 MeV states appears. Two weak groups around 6.31 MeV and 6.78 MeV are also seen at some angles.

Angular distributions for the ground state and 1.97 MeV (2^+) state are shown in Fig. 17. Notice that the ratio of the primary and secondary peaks of the ground state transition varies quite rapidly.

3.7 $^{42}Ca(^{3}He,^{7}Be)^{38}Ar$

It is immediately obvious from the size of ^{36}Ar states in the spectrum shown in Fig. 18 that the cross sections for ^{42}Ca are much smaller than those for ^{40}Ca. ^{40}Ca is only 4.96 % of the target. This small impurity is convenient for calculating the target thickness by comparison to the corresponding ^{40}Ca case.

Only three levels can be clearly resolved. These are the ground state the 2.17 MeV (2^+) and the 3.38 MeV (0^+). The excited 0^+ appears to have approximately the same cross section as the ground state. In addition a peak including the 3.81 MeV (3^-), 3.94 MeV (2^+), and the second member of the 3.38 MeV group appears. Other groups located at about 5.59 MeV, 5.82 MeV, 6.03 MeV, and 6.25 MeV cannot be associated with known states because the level density in this region is too high, although the 6.03 MeV group may contain the second member of the 5.82 MeV group.

Angular distributions (Figure 29) can only be extracted for the forward angles of the ground state. The excited states are not clear of the ^{12}C ground state at the very forward angles, while the cross section past 20° is prohibitively small for these thin targets. The angular distribution for the ground state is very forward peaked and quite similar to the ground state of ^{36}Ar. Again the ratio of the ^{7}Be states shows strong deviations from the expected value.

3.8 $^{44}Ca(^{3}He,^{7}Be)^{40}Ar$

As was the case with ^{42}Ca, the cross section for this reaction is much smaller than it was for ^{40}Ca. Even though ^{40}Ca is only 1.35% of the target the (.429) member of ^{36}Ar 1.97 states appears at all angles (Figure 19). As with ^{42}Ca this provides a convenient way to measure the target thickness relative to the ^{40}Ca target, which was measured by ^{6}Li energy loss. All known levels up to the 3.68 MeV (3^-) levels are observed. These levels are the 1.46 MeV (2^+), 2.12 MeV (0^+), 2.52 MeV (2^+), 2.89 MeV (4^+), 3.21 MeV ($1,2^+$), 3.51 MeV ($1,2^+$), and the 3.68 MeV (3^-). The fact that the 3.21 MeV and 3.51 MeV levels appear with strengths comparable to the ground state suggests that they are probably 2^+ levels.

A limited angular distribution for the ground state is shown in Fig. 29. Again the impurities and small cross sections make it impractical to extend the distribution. The angular distribution is quite similar to the ground states of the other Ar isotopes, again showing strong forward peaking.

3.9 $^{58}Ni(^{3}He,^{7}Be)^{54}Fe$, $^{60}Ni(^{3}He,^{7}Be)^{56}Fe$, $^{62}Ni(^{3}He,^{7}Be)^{58}Fe$, $^{64}Ni(^{3}He,^{7}Be)^{60}Fe$.

Spectra at 13 degrees from the four nickel isotopes studied are shown in Fig. 20. Since the Q-values are greater than for the $(^{3}He,^{7}Be)$ reaction on ^{12}C and ^{16}O, and peaks from the carbon and oxygen contaminants move relatively rapidly with angle, the Fe spectra are reasonably clean and a number of excited states are observed. In all four isotopes a strong state appears around 5 MeV. At least in ^{54}Fe it is probably a 4^{+} state. Figure 29 shows the angular distribution for this state along with the results of a finite range calculation that assumes a 4^{+} state. However, above about 2.5 MeV of excitation, the resolution is not sufficiently good to allow an unambiguous identification of a peak in the spectrum with a known iron level.

A table of the excitation energies of the peaks observed in the four iron isotopes is given (Table IV). Included in the table are the known nearby states in the corresponding isotope. The levels noted for ^{60}Fe have not previously been observed.

Angular distributions for transfers which lead to states in ^{54}Fe and ^{56}Fe are shown in Figs. 21 and 22. Only three angles were measured for ^{58}Fe and ^{60}Fe. In all cases the differential cross-sections are small, less than 4 $\mu b/sr$. Despite their small magnitude, the angular distributions still appear characteristic of a direct process with forward peaking and diffraction structure, especially

for the low lying states. The ratios of secondary to primary peaks, whenever they can be extracted, in general also appear fairly constant and around the value of 0.5. In general, the cross-sections for the heavier isotopes are smaller. For $^{64}Ni(^{3}He,^{7}Be)$ for example, all the states observed have cross-sections less than 1 $\mu b/sr$, the only exception being the ground state where the cross-section reaches 1.2 $\mu b/sr$ at 17.3°.

3.10 $^{90}Zr(^{3}He,^{7}Be)^{86}Sr$

A ^{7}Be spectrum representing states in ^{86}Sr is shown in Fig. 23. The smallness of the cross-sections is underscored by noting the size of the contaminant peaks, mindful of the fact that the 500 $\mu g/cm^{2}$ target is self supporting. Nevertheless, because of Q-value differences, low lying levels of ^{86}Sr are not obscured by the contaminants, and a number of levels in ^{86}Sr are observed as noted in Table V. Again, nearby levels known from other reactions are also listed. Above 2 MeV excitation energy, it is difficult to make a clear correspondence between observed peaks and known states in ^{86}Sr. Angular distributions are shown in Figs. 24 and 25 and again show diffraction structure even though almost all the cross-sections measured were less than 1 $\mu b/sr$.

3.12 $^{120}Sn(^{3}He,^{7}Be)^{116}Cd$, $^{124}Sn(^{3}He,^{7}Be)^{120}Cd$: Mass of ^{120}Cd.

In order to measure the previously unknown mass of ^{120}Cd and to measure the $(^{3}He,^{7}Be)$ cross-section for a target whose mass number is greater than 90, the $^{124}Sn(^{3}He,^{7}Be)^{120}Cd$ reaction was studied. Additionally the $^{120}Sn(^{3}He,^{7}Be)^{116}Cd$ reaction was measured both to calibrate the mass of ^{120}Cd and to yield additional cross-section information for heavy targets. Measurements were made at three angles. Although the cross-sections for

both reactions are less than 900 nanobarn/st, distinct ground state peaks are observed for both ^{120}Cd and ^{116}Cd (Fig. 26). The mass value and the energy levels observed are presented in Table VI and are averages of the three measurements. The measured mass excess of ^{120}Cd of -83.98±.03 MeV is in good agreement with the Garvey-Kelson[20] prediction of -83.93 MeV. On the other hand, the Myers-Swiatecki[21] prediction of -84.82 MeV is smaller by 0.84 Mev.

3.14 ^{144}Sm(^{3}He,^{7}Be)^{140}Nd, ^{206}Pb(^{3}He,^{7}Be)^{202}Hg

The experimental difficulties increase for larger masses so that an attempt to measure cross sections for the (^{3}He,^{7}Be) reaction on ^{144}Sm and ^{206}Pb was only made at 10°. The cross section for ^{144}Sm target to the ground state of ^{140}Nd was 1 μb/sr but for ^{206}Pb only an upper limit of 0.2 μb/sr could be obtained.

3.15 SUMMARY

One overview of the results may be obtained by plotting the peak differential cross-section observed as a function of atomic mass. As seen in Fig. 27, the peak cross-section drops dramatically from 70 μb/sr for ^{12}C to 8 μb/sr for ^{24}Mg. The cross-section continues to decline, though less rapidly, to less than 0.2 μb/sr for ^{206}Pb. From ^{64}Ni to ^{144}Sm the cross section has the nearly constant value of 1.0 μb/sr. The cross-section decreases smoothly with atomic mass number except for the low ^{13}C point; anomalous perhaps because, in contrast to the other targets, its mass number is odd. The overall behaviour is quite similar to the trend noted for the (d,^{6}Li) reaction by Bechetti, et al.[28]

In addition to declining with increasing target mass, the peak differential cross-section also decreases as additional neutrons are added to the target. Figure 28 plots peak differential cross-section of the ground state transitions against neutron excess. Data for several elements are included on the same plot by normalizing the data for a given atomic number so as to make the normalized value 1 for the nuclide with the smallest neutron number. The abscissa is taken to be the number of neutrons exceeding the number for the lightest isotope of the given element. In all cases measured, the peak cross section declines with neutron excess. The decrease is about the same for all elements so the effect is independent of target mass. The ^{48}Ca point is taken from Reference 14. Without a reaction theory which allows one to extract α-spectroscopic factors for neighboring nuclei, one cannot make a quantitative statement on the effect of excess neutrons. However the consistency of the effect for various isotopic chains seems to imply that excess neutrons tend to dilute α-particle clusters on the nuclear surface. Calculations by Kurath and Towner[22] in the fp shell do suggest such a blocking effect with excess neutrons in the nickel isotopes.

4. Distorted Wave Calculations

For the (^{3}He,^{7}Be) reaction to be used as a tool to study particle clustering on the nuclear surface, a reaction theory is required to permit separation of kinematic and structure effects, especially for different nuclei. If we assume that the 4 nucleons are transferred as an S=0, T=0 cluster, the cross section for the pickup process B(b,a)A may be written

$$\frac{d\sigma}{d\Omega}(\theta) = \frac{2Sa+1}{2Sb+1} \sum_{\ell} (2\ell+1) W^2(\ell_1 \ell_1 \ell_2 \ell_2; 0\ell) S_1 S_2 \sigma_\ell(\theta)_{DW} \qquad 4.1$$

where S_a, the spin of ^{7}Be, is 3/2, S_b, the spin of ^{3}He, is 1/2, ℓ_1 and ℓ_2 are the orbital angular momenta of the α-particle in the ^{7}Be(a) and target nucleus (B) respectively. W is a Racah coefficient and ℓ is the orbital angular momentum transferred in the reaction. Note that the sum over ℓ's is an incoherent sum. With the assumption of transfer of an α-particle cluster, the spectroscopic factors S_1 and S_2 can be factored out. S_1 refers to the spectroscopic factor for the α-particle combined with ^{3}He in ^{7}Be and S_2 the spectroscopic factor for the states in the final nucleus. The value of S_1 is assumed to be unity in order to extract values of S_2. The term σ_{DW} was calculated using the computer code, LOLA and LOLITA[11] which takes account of recoil effects. Since the ^{3}He and α-particles in ^{7}Be cannot be in a relative ℓ=0 state, the zero range approximation, often employed in distorted wave calculations, is not valid in this case. The code LOLA makes no such approximation.

It should be noted also that in finite range, the parity selection rule, which restricts the α-transfer allowed in the reaction, does not apply. Thus all α-transfer values allowed by angular momentum conservation rules[11] must be included in the finite range calculations.

However, the excitation of unnatural parity states (with $\pi = (-1)^{J+1}$) in the final nucleus is not allowed in a pure α-particle transfer reaction on an even-even nucleus. The reason is that the target bound state, consisting of the final state and the α-particle

with $J^\pi = 0^+$ cannot be formed unless the parity of the final state is $(-1)^J$. Suppose the final state has spin-parity J^π and the α-particle is formed with orbital angular momentum L, then L must equal J to form the 0^+ target ground state. The overall parity of the target state is positive so that the parity of the final state must equal $(-1)^J$. Thus the extent to which unnatural parity states are excited gives an indication of the breakdown of the simple α-cluster transfer description of the reaction.

Another feature of the reaction which follows from equation 4.1 is that, because the wave functions of the ground state and first excited state of ^{7}Be are so similar, the cross-sections for reaching these states should be proportional to the factor $(2S_a+1)$ where S_a is the spin of the state in ^{7}Be. Therefore, the ratio of the cross-sections for reaching the excited $1/2^-$ state should be one half the cross-section for the ground state $(3/2^-)$. As noted in the previous section, the ratio of cross-sections for the secondary to the primary peak is not always 0.5, especially for the lighter nuclei. These differences imply either a more complex reaction mechanism or the existence of some unexpected spin dependence in the optical or interaction potentials. Unless otherwise noted, all the LOLA calculations are compared with the differential primary (ground state) peak of ^{7}Be.

In order to perform the LOLA calculations, optical model parameters are needed for both the entrance and exit channels. Optical model parameters for elastic scattering of ^{3}He from the various target nuclides are available, however, only for energies somewhat lower than the 70 MeV bombarding energy of the present work. When possible the parameters used are taken from Doering,

et al.[23] since their work was done at 70 MeV. A folding model was used for the ^{12}C, ^{13}C and ^{16}O cases. The folding model parameters were checked against the data of Benenson, et al.[24] who studied the elastic scattering of 70 MeV ^{3}He on ^{13}C. The agreement was very good. Since ^{7}Be has a half life of only 53 days, ^{7}Be beams are unavailable. Therefore, ^{7}Be elastic scattering data, from which optical model parameters are deduced, does not exist. In the absence of ^{7}Be parameters, ^{7}Li optical parameters are used instead. Unfortunately the ^{7}Li parameters available are for substantially lower energy than the 50 to 60 MeV ^{7}Be's in the present experiment. Although the ^{7}Li complex optical potential, which does significantly affect the magnitude of the cross-section calculated by LOLA, should probably be increased when applied to ^{7}Be to allow for greater absorption of the more weakly bound ^{7}Be, because of the other uncertainties no adjustment was made. Any such change would be negligible compared to the inherent uncertainty in the parameters. For many cases, several sets of parameters have been tried. A list of the parameters which give at least fair fits to the data are listed in Table VII.

Reaction calculation have been executed and α-spectroscopic factors determined for $^{8}Be(0^+,2^+,4^+)$, $^{9}Be(3/2^-,5/2^-)$, $^{12}C(0^+,2^+)$, $^{20}Ne(0^+,2^+,4^+)$, $^{22}Ne(0^+,2^+,4^+)$, $^{36}Ar(0^+,2^+)$, $^{38}Ar(0^+)$, $^{40}Ar(0^+)$, $^{54}Fe(0^+,2^+,4^+,2^+)$, $^{56}Fe(0^+,2^+,4^+)$, and $^{86}Sr(0^+,2^+,2^+)$. Data and calculations are displayed in Fig. 29.

For many cases, even with the uncertainties in the optical parameters, fairly good fits to the data are obtained. This is true for example for the ground states of ^{8}Be, ^{12}C, ^{36}Ar, ^{54}Fe, ^{56}Fe and ^{86}Sr and the 2^+ state of ^{8}Be.

The fits to the 0^+, 2^+, and 4^+ ^{8}Be data are generally quite good. For the 0^+ the calculation falls too rapidly at angles greater than 20°. The minima and maxima of the 2^+ calculations occur at angles that differ from the data by about 7°.

The angular distributions for the $^{9}Be(3/2^-)$ and $^{9}Be(5/2^-)$ are not reproduced by the calculation. Examination of the ℓ=1,2 and 3 components that are summed to obtain the calculated results shows that the fit is destroyed by the ℓ=1 contribution. The pure ℓ=3 fit is shown in Fig. 30. A much better fit is obtained.

The ^{12}C ground state and 4.44 MeV level are well reproduced by the DWBA calculations. The spectroscopic factor for the ground state is 2.93 which is about the same as for the ^{8}Be ground state.

The calculations for the ^{20}Ne and ^{22}Ne states are in general poor. In many cases a shifting of the prediction by about 10° to larger angles would improve the fit greatly. Calculations for corresponding states in the two isotopes are quite similar, however the data exhibit significant differences. The spectroscopic factors are smaller than the ^{12}C factors by about a factor of 100.

The calculations for ^{40}Ca ground state produces a nice fit, while the data for the 2^+ rises to rapidly in the forward angles. The spectroscopic factors here are significantly larger than they were for the Ne isotopes.

Spectroscopic factors have also been extracted from the forward angle data for $^{42,44}Ca$. The same set of optical parameters

was used for all the Ca isotopes. The blocking effect can be clearly seen, as the spectroscopic factors for $^{42,44}Ca$ are smaller than that for ^{40}Ca by about a factor of ten.

The calculations for the Fe isotopes are quite successful. An outstanding example is the ^{54}Fe ground state. As was the case with the Ne isotopes the calculation does not change much for the different isotopes. The spectroscopic factors for $^{54,56}Fe$ are quite small being about .003 on the average.

The ^{86}Sr 1.078 MeV (2^+) state is another example of a very good fit. The spectroscopic factors for the three states seen here are larger than they were for the Fe isotopes.

The absolute values of the spectroscopic factors obtained are probably not significant for a number of reasons. First of all, we have assumed that the spectroscopic factor for an particle in ^{7}Be is exactly unity. While this is a reasonably good assumption, smaller values would mean larger S's for the residual nuclei. In addition, no normalization was used in the reaction theory and it would be surprising if none were needed considering the experience with other multi-nucleon transfer reactions such as (p,t).[25] Finally the absolute cross-sections calculated depend strongly on both the optical parameters (the calculated cross-section for example can vary by as much as a factor of 10 for a 50% increase in the depth of the imaginary part of the ^{7}Be optical potential) and on the bound state geometry. However the relative spectroscopic factors obtained from calculated cross-sections with the same families of optical potentials and the same bound state geometrical factors probably do have some significance. A list of relative S's (assuming a value of 1.0 for the ground state of ^{7}Be) is given in Table VIII.

While any conclusions drawn from these values of S_α must only be tentative because of the uncertainties remaining in the cross-section calculation, it does appear that the present results are not consistent with earlier reports of maximum alpha clustering from carbon to lead from $(\alpha,2\alpha)$ studies.[3] The present data suggest that S_α for ^{24}Mg is about (250) times smaller than for ^{12}C and the S_α's for ^{58}Ni are also about (250) times smaller than for ^{12}C. Although the S_α values do not appear to change very much between ^{58}Ni and ^{90}Zr they may even increase slightly. Martin, et al.[5] found reasonably constant S_α's from ^{40}Ca to ^{114}Sn using the $(d,^{6}Li)$ reaction. Studies of the $(^{3}He,^{7}Be)$ reaction[7] and the $(d,^{6}Li)$ reaction[4] on ^{12}C and ^{16}O suggest that the S_α's for these two cases are approximately the same, at least within a factor of two or three which is consistent with the present results. Further comparisons are probably not too significant since different nuclei were studied, although the 30 MeV $(^{3}He,^{7}Be)$ data[7] seem to imply more constant S values from ^{12}C to ^{40}Ca than are suggested by the present experiment.

The data seem to show anomolously large spectroscopic factors for the doubly magic nuclei. The targets ^{12}C, ^{16}O, ^{40}Ca, and ^{90}Zr give spectroscopic factors that are larger than the neighboring nuclei. This result shows a marked contrast with the $(d,^{6}Li)$ survey of reference 28, where the S_α's for closed shell nuclei were anomolously low. In addition all of the spectroscopic factors in the $(d,^{6}Li)$ survey were roughly the value found for ^{16}O, which does not reproduce the sharp decrease which is observed here.

Unfortunately more nuclei would have to be studied to make a more definitive statement.

Kurath[26] has calculated a number of S_α values for a number of 0p shell nuclei and again the present results are reasonably consistent with these predictions for the cases that can be directly compared. For example the ratio of calculated S_α values for ^{16}O compared to ^{12}C is 0.42, which is to be compared with the value of 0.47 in Table VIII. Again the ratio of S_α's for the $^{12}C(2^+)$ state compared to the ground state is 2.4 and the value from the present experiment is 4.5. Thus the general trends predicted by the Kurath calculations are shown by the present results and given the uncertainties in the specific values are quite consistent with the theoretical predictions.

5. CONCLUSIONS

This survey of the (^3He,^7Be) reaction suggests that this reaction is potentially an important technique for the study of α-clustering on the nuclear surface. At higher bombarding energies, it is possible to examine a number of states in the same nucleus up to reasonably high excitation energy. The peak cross-sections do drop rapidly with increasing A (and increasing N for a series of isotopes) but even up to A=140 the peak cross-sections are about 0.5 to 1 μb/sr.

The reaction does appear to be direct and no strong evidence has been found to contradict the previous conclusions that it proceeds mainly by the transfer of an α-cluster. Primary (ground state) and secondary (0.429 MeV) angular distributions for a given level are generally quite similar. The ratio of cross-sections in

many cases, however, departs from the constant value of 0.5 as expected from a simple model. The explanation for this discrepancy and the sensitivity of the transfer hypothesis to these departures are not clear. Unnatural parity states are observed in this reaction in a number of nuclei but tend to be weaker than the natural parity states.

Assuming an α-cluster transfer, the comparison of the experimental cross-sections with calculations using the code LOLA, yields α-spectroscopic factors for a number of nuclei. This prescription seems to have problems with ^{13}C that are not explained, but seems to work well for even-even targets. While little reliance can be placed on the absolute S_α's, the value relative to ^{12}C show a definite decrease down to .02 for ^{24}Mg, then remaining constant to ^{90}Zr. If these relative values can be relied upon, then the implication is that the amount of clustering on the nuclear surface is the same for heavy nuclei as for lighter nuclei. The S_α for ^{40}Ca is .12 suggesting that doubly closed nuclei may exhibit more α-clustering than the average.

Finally, the mass excess of ^{120}Cd (-83.98±.03 MeV) was determined and a number of new energy levels for this nucleus as well as for ^{60}Fe were obtained.

REFERENCES

1. D.H. Wilkinson, Comments on Nuclear and Particle Physics 1, 36(1967).
2. C.E. Wiegand, Phys. Rev. Letters 22, 1235(1969).
3. G.Igo, L.F.Hansen and T.J. Gooding, Phys. Rev. 131, 337(1963).
4. H.H.Gutbrod, H.Yoshida and R. Bock, Nucl. Phys.A165 240(1971).
5. P. Martin, J.B. Viano, J.M. Loiseaux and Y. Le Chalony, Nucl. Phys. A212, 304(1973).
6. J.R. Comfort, W.J. Braithwaite, J.R. Duray, H.T. Fortune, W.J. Courtney and H.G. Bingham, Phys. Lett. 40B, 456(1972).
7. C.Detrax, H.H. Duhm and H.Hafner, Nucl. Phys. A147, 488(1970).
8. C. Detraz, C.D. Zafiratos, C.E. Moss and C.S. Zaidins, Nucl. Phys. A177, 258(1971).
9. C.D. Zafiratos, C. Detraz, C.E. Moss and C.S. Zaidins, Phys. Rev. Letters 27, 437(1971).
10. C. Detraz, C.D. Zafiratos, H. Rudolf and C.S. Zaidins, Phys. Rev. Letters 28, 117(1971).
11. R.M. deVries, Phys. Rev. C8, 951(1973).
12. D.L.Bayer, Michigan State University Report MSUCL-34(unpublished).
13. R.W. Ollerhead, G.F.R. Allen, A.M. Baxter, B.W.J. Gillespie and J.A. Kuehner, Can J. of Physics 49, 594(1971).
14. W.F. Steele, P.A. Smith, G.M. Crawley and S. Maniipau, to be published.
15. J.M. Moss, D.L. Hendrie, C. Glashausser and J. Thirion, Nucl. Phys. A194, 12(1972).
16. G.S. Mani, Nucl. Phys. A165, 225(1971).
17. G.S. Mani, Nucl. Phys. A169, 194(1971).
18. W.F. Steele, Ph.D. Thesis, Michigan State University, 1974 (unpublished).

19. A.V. Ramayya, B. Can Nooijen, J.W. Ford, D. Krompotie, J.H. Hamilton, J.J. Pinajran and N.R. Johnson, Phys. Rev. C2,2248(1970).
20. G.T. and I. Kelson, Phys. Rev. Letters 16, 197(1966). G.T. Garvey, W.J. Gerace, R.L. Jaffe, I. Talmi and I. Kelson, Rev. Mod. Phys. 41, 51(1969).
21. W.D. Myers and W.J. Swaitecki, Lawrence Radiation Lab. Report- UCRL - 11980 (1965, unpublished).
22. D. Kurath and I.S. Towner, Nucl. Phys. A222, 1(1974).
23. R.R. Doering and W. Benenson, A.I. Galonsky and R.A. Hinrichs, Journal of Comp. Phys. 12, 498(1973).
24. H.W. Boer, J.J. Kraushaar, C.E. Moss, N.S.P. King, R.B.L. Green, P.D. Kung and E. Rost. Annals of Phys. 76, 437(1973).
25. D. Kurath, Phys. Rev. C7, 1390(1973).
26. G. Audi, C. Detraz, M. Largevin and F. Pougheon, Nucl. Phys. A237, 300(1974).
27. F.D. Becchetti, L.T. Chua, J. Jänecke, and A.M. Vandermolen, Phys. Rev. Letters 34, 225(1975).
28. P. Schumacher, N. Veta, H.H. Duhm, K.I. Kubo, and W.J. Klages, Nucl. Phys. A212, 573(1973).
29. K.I. Kubo and M. Hirata, Nucl. Phys. A187, 186(1971).
30. C.B.Fulmer and M. Hirata, Phys. Rev. C5, 1969(1972).
31. K.I. Kubo, H.H. Duhm and N. Veta, Phys. Lett. 45B, 299(1973).
32. C.B. Fulmer, J.C. Hafele, and C.C. Foster, Phys. Rev. C8, 200(1973).

Table I.--Target Information.

Target	Thickness ($\mu g/cm^2$)	Chem. form	backing	Isotopic Purity
^{12}C	100	carbon	none	natural abundance
^{13}C	200	carbon	none	
^{16}O	53	WO_3	250$\mu g/cm^2$ Au	natural abundance
^{24}Mg	300	metal	none	
^{26}Mg	250	metal	none	
^{40}Ca	375	metal	carbon	natural abundance
	50	metal	carbon	natural abundance
^{42}Ca	100	metal	carbon	94.42
^{44}Ca	90	metal	carbon	98.56
^{58}Ni	275	metal	none	99.86
^{60}Ni	218	metal	none	99.79
^{62}Ni	260	metal	none	98.83
^{64}Ni	250	metal	none	98.02
^{90}Zr	500	metal	none	
^{120}Sn	525	metal	none	98.39
^{124}Sn	290	metal	none	96.00
^{144}Sm	250	metal	carbon	
^{206}Pb	500	metal	carbon	

Table II.--Energy Levels in ^{8}Be

E_x	Γ(keV)	J^π	Peak $d\sigma/d\Omega$($\mu b/sr$) for primary peak
0.00	6.8 eV	0^+	70
2.9	1560	2^+	140[a]
11.4	7000	4^+	24[a]
16.63	107	2^+	9
16.91	77	2^+	12[b]
17.64	10.7	1^+	3.5
18.15	138	1^+	Not seen
18.91	48	2^-	
19.06	270	3^+	

a. Since both primary and secondary peaks are included, 2/3 of the observed value is given.

b. Since only the secondary peak is observed, twice the measured value is given.

Table III.--Energy levels in ^{22}Ne.

J^{π} [a]	E_x(MeV) [a]	$E_x \pm \Delta E_x$(MeV) [b]
0^+	0.00	0.00
2^+	1.27	1.27 ± 0.03
4^+	3.36	3.35 ± 0.04
2^+	4.46	4.47 ± 0.05
2^-	5.14	
	5.33	
	5.36	
4^+	5.52	5.57 ± 0.16
(3^+)	5.64	
2^+	5.92	
(3^-)	6.12	6.00 ± 0.17
0^+	6.24	
6^+	6.35	6.42 ± 0.17
		7.52 ± 0.20
		$8.30 \pm .27$
		$8.75 \pm .35$
		$9.15 \pm .40$
		$9.82 \pm .75$

a. From Ref. 13.

b. Present results.

Table IV.--Energy Levels of Iron Isotopes.

1. Energy Levels observed in ^{54}Fe

J^{π} [a]	E_x(MeV) [a]	Present Work, E_x(MeV)
0^+	0.0	0.0
2^+	1.409	$1.41 \pm .01$
4^+	2.540	$2.53 \pm .02$
0^+	2.654	
6^+	2.948	$2.96 \pm .02$
2^+	2.959	
2^+	3.164	
3^-	4.70 [b]	$4.80 \pm .04$
	4.78	
4^+	4.95	$5.72 \pm .25$

2. Energy levels observed in ^{56}Fe

J^{c}	E_x(MeV) [c,d]	Present Work, E_x(MeV)
0^+	0.0	0.0
2^+	0.849	$0.85 \pm .01$
(4^+)	2.085	$2.06 \pm .02$
2^+	2.695	$2.63 \pm .05$
$(0^+,2^+)$	2.986	$3.07 \pm .03$
4^+	3.159	
$(2^+,6^+)$	3.411	
2^+	3.635	$3.59 \pm .06$
4^+	4.860	$4.85 \pm .05$
4^+	5.880	$5.87 \pm .06$

Table IV.--cont.

3. Energy levels observed in ^{58}Fe

J^{π} [e]	E_x(MeV) [e]	Present Work, E_x(MeV)
0^+	0.0	0.00
2^+	0.814	$0.812 \pm .003$
2^+	1.684	$1.659 \pm .011$
4^+	2.085	$2.081 \pm .012$
4^+	2.619	$2.573 \pm .012$
3^-	2.970	$3.03 \pm .04$
2^+	2.08	
2^+	3.522	$3.57 \pm .02$
3^-	3.845	$3.88 \pm .02$
		$5.39 \pm .03$

4. Energy levels in ^{60}Fe

Present Work, E_x (MeV)	Present Mass Excess (MeV)	Previous Mass Excess (MeV)
0.00	$-61.437 \pm .010$	$-61.434 \pm .030$
$0.835 \pm .010$		
$2.11 \pm .02$		
$3.08 \pm .01$		

a. Ref. 15.
b. 10 levels not listed here.
c. Ref. 16.
d. All levels observed are not listed here.
e. Ref. 17.

Table V.--Energy levels observed in ^{86}Sr

J^{π} [a]	E_x(MeV) [a,b]	Present Work, E_x(MeV)
0^+	0.00	0.0
2^+	1.077	$1.09 \pm .02$
2^+	1.854	$1.84 \pm .02$
4^+	2.230	$2.23 \pm .05$
5^-	2.673	$2.71 \pm .07$
	2.788	
3^-	2.977	
$(4,5)^-$	3.056	$3.03 \pm .07$
$(3)^-$	3.185	
$(3^+,4^+)$	3.362	$3.44 \pm .08$
	3.500	
	3.97	$3.96 \pm .08$
	4.15	

a. From Ref. 19.
b. Not all levels given in ref. 19 are listed here.

Table VI.--Mass and energy levels of ^{120}Cd.

Level	Mass Excess(MeV)	Excitation Energy (MeV)
1	$-83.98 \pm .03$	0.0
2	$-83.48 \pm .05$	0.50
3	$-82.68 \pm .04$	1.30

Table VII.--Optical Parameters.

Reaction	Ref.	V	R_r	A_R	W_{vol}	W_{sur}	R_I	A_I
$^{12}C(^3He,^7Be)$	a	120.0	1.16	.933	12.8	42.4	1.28	.819
	b	245.0	1.21	.759	14.7		2.00	.909
$^{13}C(^3He,^7Be)$	a	120.0	1.16	.933	12.8	42.4	1.28	.819
	c	187.8	1.208	.8424	12.9		2.17	.770
^{16}O	a	120.0	1.16	.933	12.8	42.4	1.28	.819
	c	187.8	1.208	.824	12.9		2.17	.770
^{24}Mg	d	114.0	1.15	0.826		75.2	1.18	.820
	e	88.0	1.30	.800	8.5		1.90	.700
^{26}Mg	d	114.0	1.15	.826		75.2	1.18	.820
	e	88.0	1.30	.800	8.5		1.90	.700
^{58}Ni	f	126.5	1.12	.837		81.6	1.26	.841
	g	152.0	1.32	.790	3.65		2.48	.490
^{60}Ni	f	126.5	1.12	.837		81.6	1.26	.841
	g	152.0	1.32	.790	3.65		2.48	.490
^{90}Zr	f	126.5	1.12	.836		81.6	1.26	.841
	h	152.0	1.42	.710	10.24		1.88	.520

a. Ref. 23.
b. Ref. 28.
c. Ref. 31.
d. Ref. 30
e. Ref. 29
f. Ref. 32
g. Ref. 33.
h. Ref. 33.

Table VIII.--Alpha particle spectroscopic factors.

Target	0^+	2^+	4^+	Normalized[a]	S (30MeV)[e]	S (26MeV)^f_A	S (26MeV)^f_B	S (26MeV)^f_C	S (26MeV)^f_D
^{12}C	3.008	6.484	2.242	1.0	1.0	1.0	1.0	1.0	1.0
^{13}C[b]	1.326	.220	-	.44					
^{16}O	2.929	5.920	-	.97	3.3	0.55	0.85	0.45	0.7
^{24}Mg	0.013	0.026	0.019	.004					
^{26}Mg	0.020	0.026	0.007	.007					
^{40}Ca	0.123	0.123		.04	0.67	0.8	2.0	0.09	1.0
^{42}Ca	0.017			.006					
^{44}Ca	0.015			.005					
^{58}Ni	0.011	0.008	0.008	.004					
^{60}Ni	0.008	0.007	0.001[c] 0.018	.003					
^{90}Zr	0.024	0.042[d] 0.016	0.021	.008					

a. Normalized to ^{12}C ground state transition.

b. 0^+ and 2^+ entries are $3/2^-$ and $5/2^-$.

c. 0.001 is for the 2.118 MeV state. 0.018 is for the 4.86 MeV group.

d. 0.042 is for the 1.078 MeV state. 0.016 is for the 2.232 MeV (2^+) state.

e. From Ref. 7.

f. From Ref. 27.

FIGURE CAPTIONS

Figure 1.--The counter arrangement and logic used to separate the $^7Be^+$ ions from the other reaction products.

Figure 2.--A typical time of flight spectrum. ^{12}C was the target for this particular case.

Figure 3.--Three spectra from $^{12}C(^3He, ^7Be)^8Be$. The bottom spectrum shows the high excitation region. The broad 4^+ level at 11.4 MeV shows clearly in the 22 degree spectrum.

Figure 4.--The angular distributions for the primary and secondary peaks that correspond to the ground state and 17.64 MeV (1^+) state of ^8Be are shown with the ratios of the individual points. A simple α-transfer predicts the ratio to be 0.5 at all angles. The curves are the result of interpolation between the points. They are shown for visual convenience only.

Figure 5.--The angular distributions for the ^8Be states where the primary and secondary peaks can not be resolved.

Figure 6.--The $^{13}C(^3He, ^7Be)^9Be$ spectra at 8.5° and 40°. Notice the appearance of three strong broad peaks in the 40° spectrum.

Figure 7.--The angular distributions for the primary and secondary peaks corresponding to the ground state and 2.429 MeV state of ^9Be are shown along with the ratio.

Figure 8.--The 20 spectrum of $^{16}O(^3He, ^7Be)^{12}C$.

Figure 9.--The angular distributions and ratios for the ground states and 4.44 MeV state of ^{12}C.

Figure 10.--The $^{24}Mg(^{3}He,^{7}Be)^{20}Ne$ spectrum taken at 27.5°.

Figure 11.--The angular distribution for the 4.97 MeV (2^-) level of ^{20}Ne. The simple α-transfer does not allow the population of unnatural parity states.

Figure 12.--The angular distribution and ratios for the states observed in the $^{24}Mg(^{3}He,^{7}Be)$ reaction.

Figure 13.--The 45° spectrum of $^{24}Mg(^{3}He,^{7}Be)^{22}Ne$.

Figure 14.--The angular distributions and ratios for states observed in the $^{26}Mg(^{3}He,^{7}Be)^{22}Ne$ reaction.

Figure 15.--Angular distributions for 5.52 MeV (4^+) and 5.92 MeV (2^+) levels of ^{22}Ne. The 5.92 MeV peak also contains the 5.52 MeV secondary peak.

Figure 16.--The $^{46}Ca(^{3}He,^{7}Be)^{36}Ar$ spectrum at 26° .

Figure 17.--The angular distributions and ratios for the ground state and 1.97 MeV (2^+) states of ^{36}Ar.

Figure 18.--The 18° spectrum for $^{42}Ca(^{3}He,^{7}Be)^{38}Ar$.

Figure 19.--The $^{44}Ca(^{3}He,^{7}Be)^{40}$ Ar spectrum at 18 .

Figure 20.--The 13° spectra for $^{58,60,62,64}Ni(^{3}He,^{7}Be)^{54,56,58,60}Fe$.

Figure 21.--The angular distributions and ratios for the levels observed in the $^{58}Ni(^{3}He,^{7}Be)^{54}Fe$ reaction.

Figure 22.--The angular distributions and ratios observed in the $^{60}Ni(^{3}He,^{7}Be)^{56}$ Fe reaction.

Figure 23.--The 21° spectrum of $^{90}Zr(^{3}He,^{7}Be)^{86}Sr$.

Figure 24.--Angular distributions and ratios for the ground state and 1.078 MeV (2^+) state of ^{86}Sr.

Figure 25.--Angular distributions for levels of ^{86}Sr for which the secondary peak was unresolved. Since each of these levels is separated from its neighbor by about 400 keV it is likely that they represent combined primary and secondary peaks.

Figure 26.--Spectra for $^{120}Sn(^{3}He,^{7}Be)^{116}Cd$ at 10° and $^{124}Sn(^{3}He,^{7}Be)^{120}$ Cd at 13°.

Figure 27.--The maximum cross section observed for each target is plotted against the target mass.

Figure 28.--The peak cross section for the isotope chains $^{12,13}C$, $^{24,26}Mg$, $^{40,42,44,48}Ca$, $^{58,60,62,64}Ni$, $^{120,124}Sn$ are plotted against neutron excess. The cross section is relative to the cross section of the smallest neutron excess in the chain. Thus the Sn point is the ratio of ^{124}Sn to ^{120}Sn.

Figure 29.--A comparison of finite range calculations, assuming an α-cluster transfer, and the data.

Figure 30.--The ℓ=3 component of the finite range calculation The normalization is for the best fit with this component only.

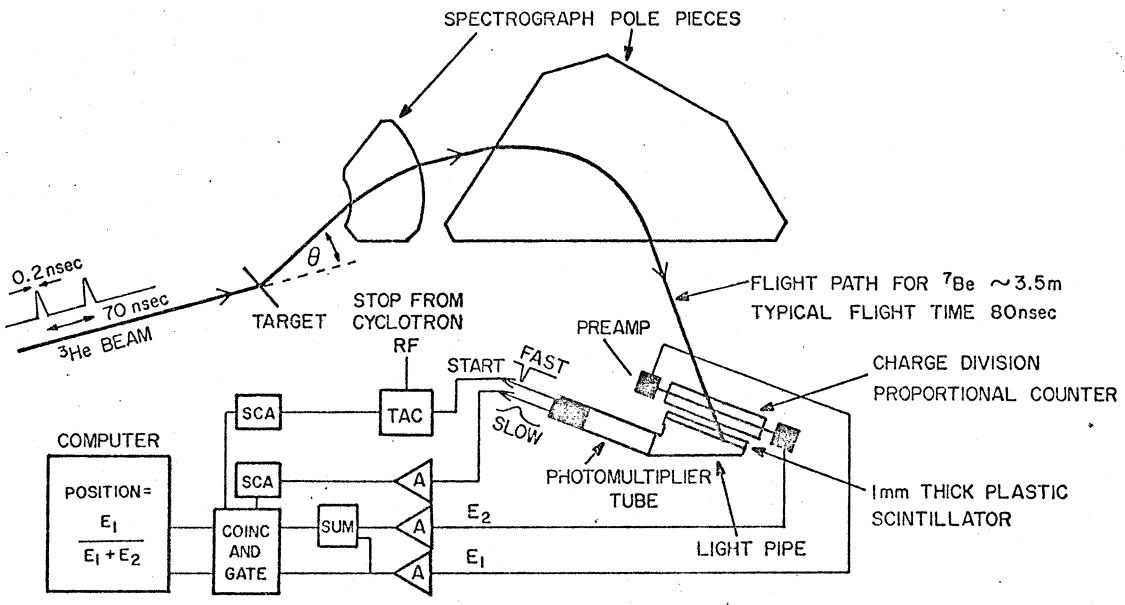

TIME OF FLIGHT PARTICLE IDENTIFICATION IN THE SPECTROGRAPH

Fig. 1

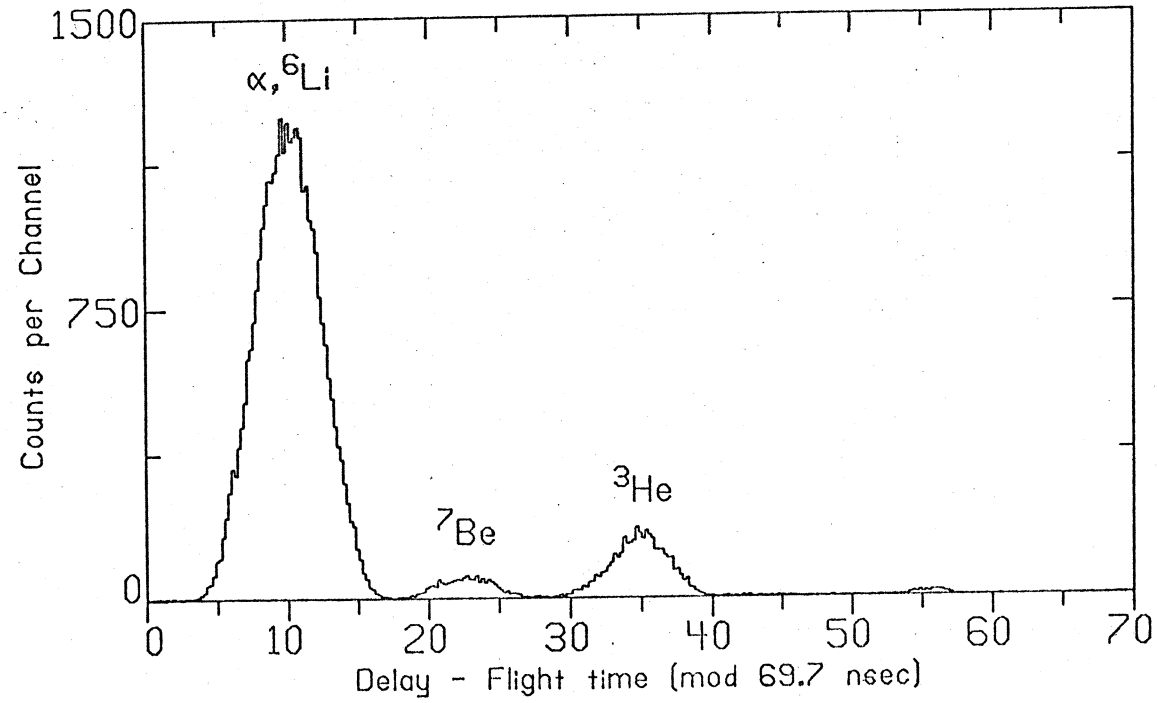

Fig. 2

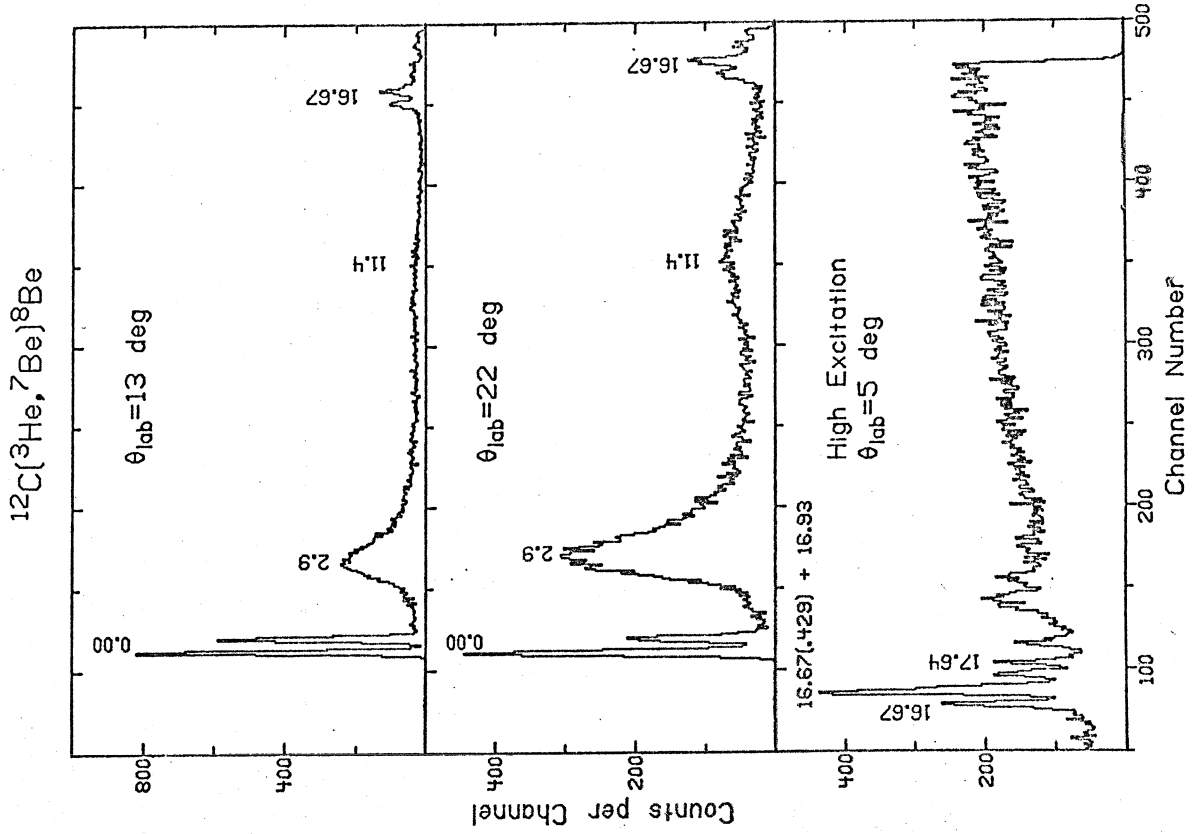
$^{12}C(^3He,^7Be)^8Be$
θ_{lab}=13 deg
θ_{lab}=22 deg
High Excitation
θ_{lab}=5 deg
0.00
2.9
11.4
16.67
16.67(.429) + 16.93
17.64
Counts per Channel
Channel Number

Fig. 3

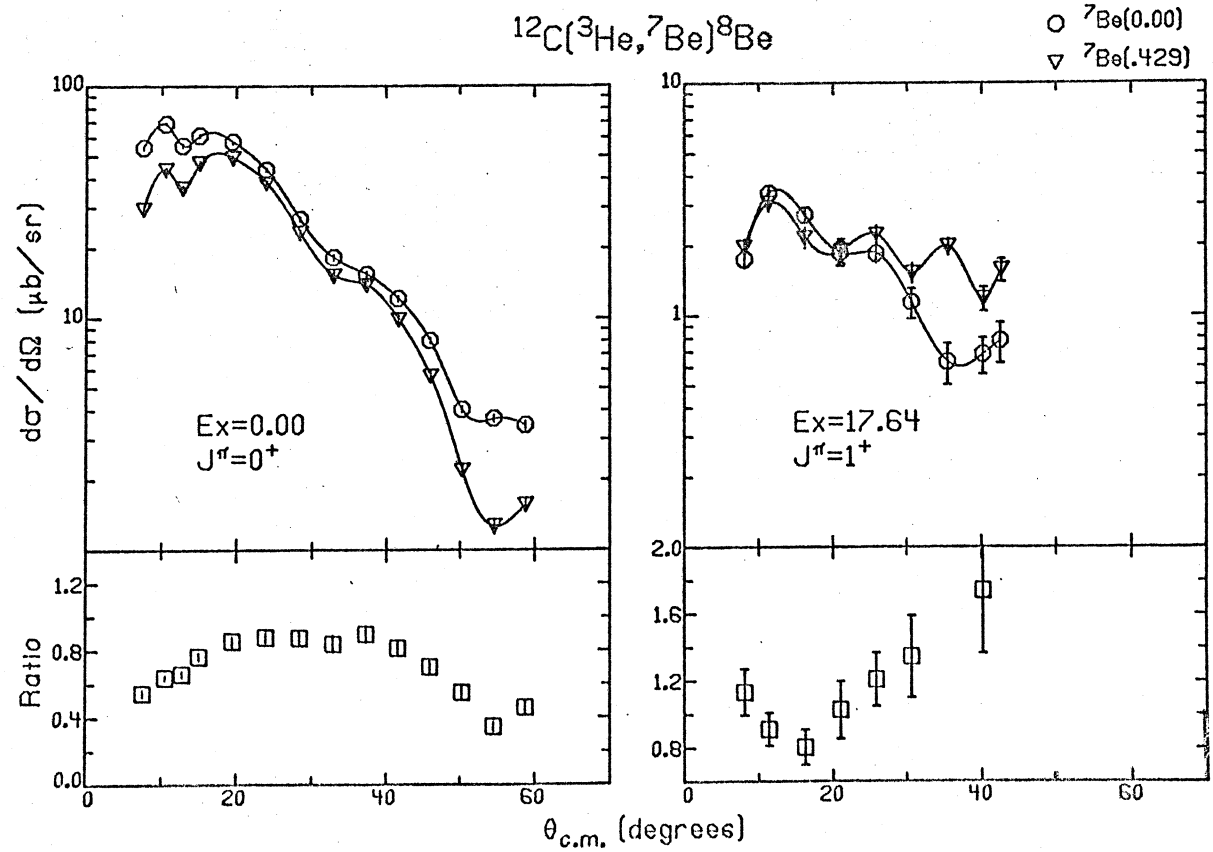
$^{12}C(^3He,^7Be)^8Be$
○ ^7Be(0.00)
▽ ^7Be(.429)
$d\sigma/d\Omega$ (μb/sr)
Ex=0.00
$J^\pi=0^+$
Ex=17.64
$J^\pi=1^+$
Ratio
$\theta_{c.m.}$ (degrees)

Fig. 4

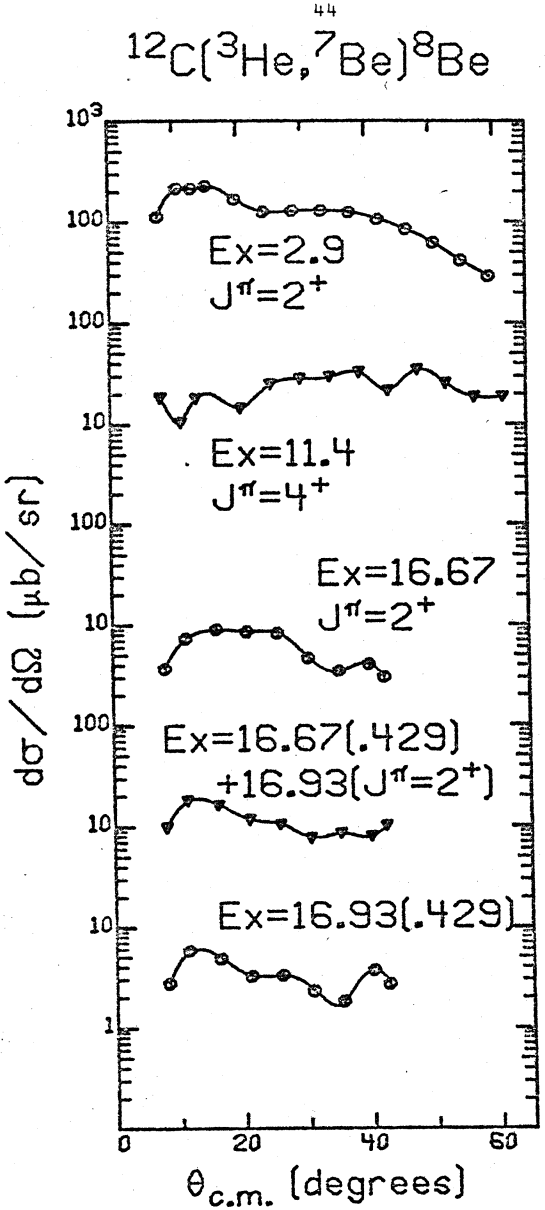
$^{12}C(^{3}He,^{7}Be)^{8}Be$
Ex=2.9
$J^{\pi}=2^{+}$
Ex=11.4
$J^{\pi}=4^{+}$
Ex=16.67
$J^{\pi}=2^{+}$
Ex=16.67(.429)
+16.93($J^{\pi}=2^{+}$)
Ex=16.93(.429)
$d\sigma/d\Omega$ (μb/sr)
$\theta_{c.m.}$ (degrees)

Fig. 5

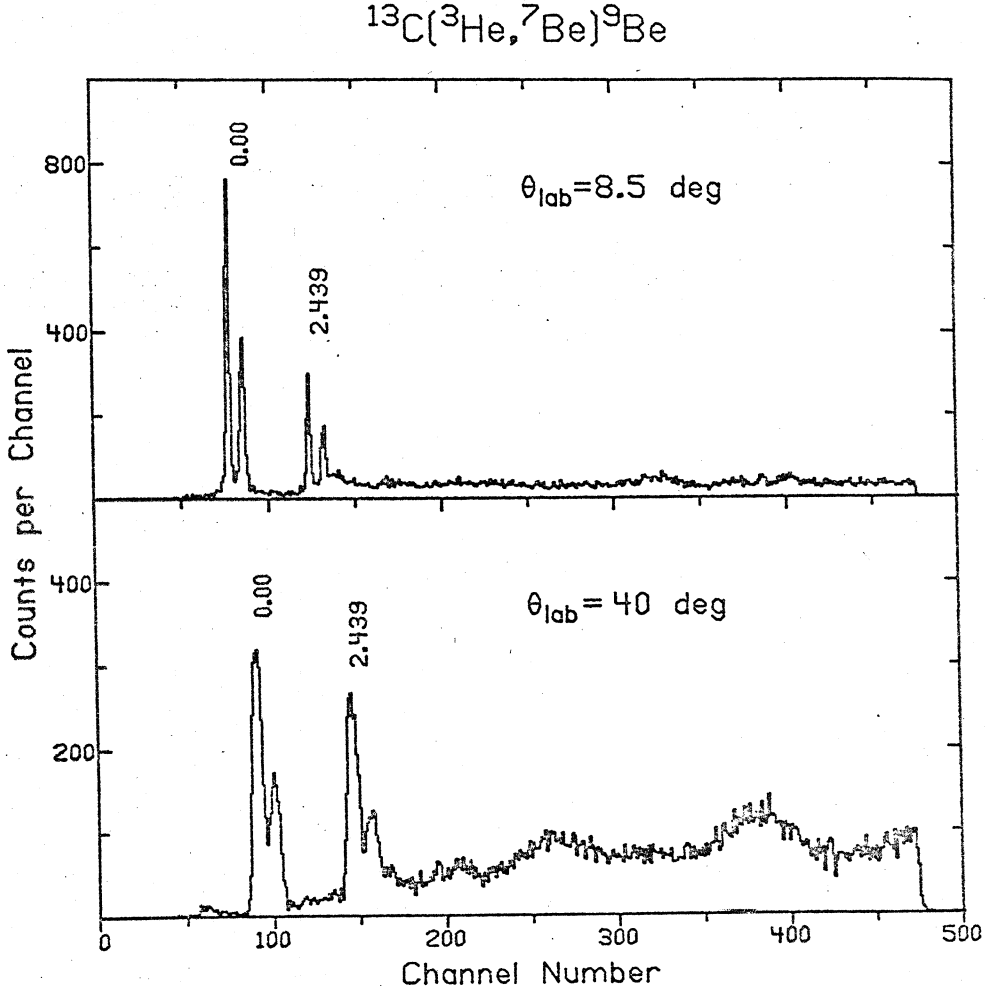
$^{13}C(^{3}He,^{7}Be)^{9}Be$
0.00
2.439
θ_{lab}=8.5 deg
0.00
2.439
θ_{lab}= 40 deg
Counts per Channel
Channel Number

Fig. 6

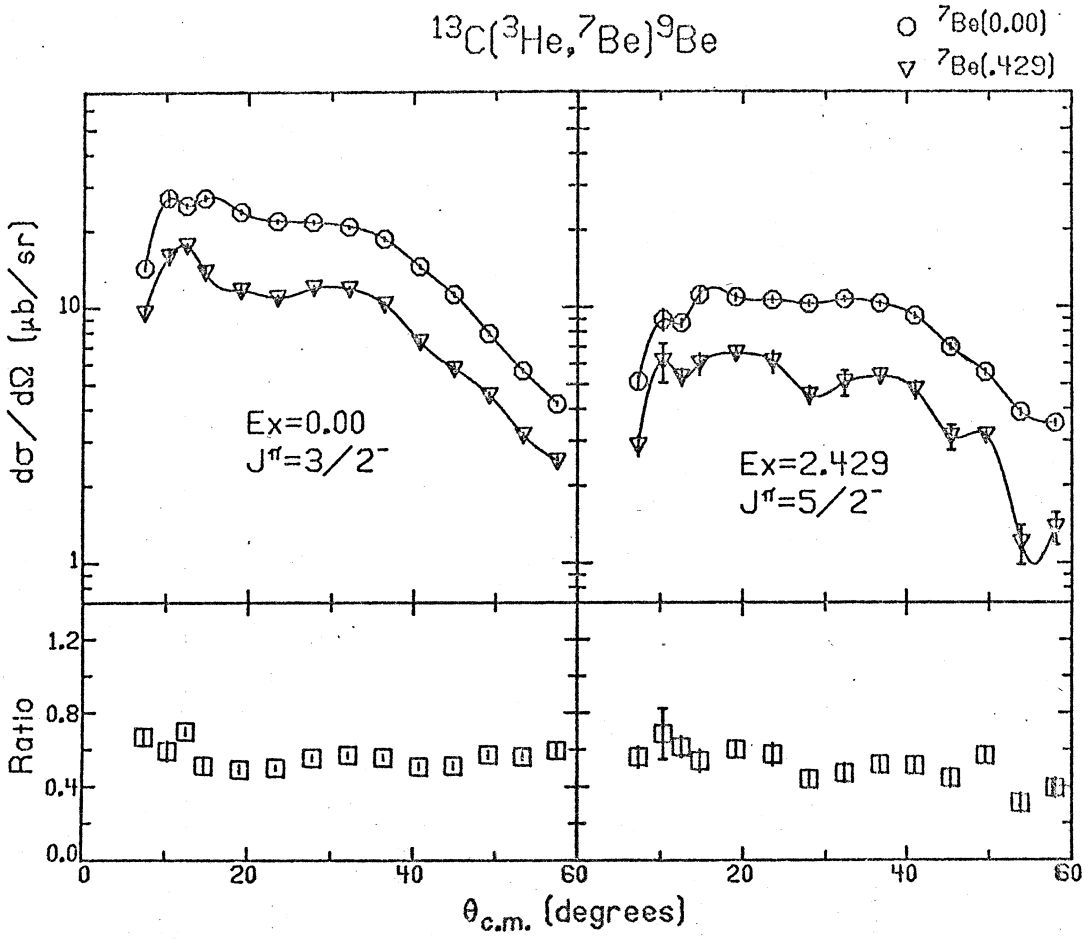
$^{13}C(^{3}He,^{7}Be)^{9}Be$
○ $^{7}Be(0.00)$
▽ $^{7}Be(.429)$
dσ/dΩ (μb/sr)
Ex=0.00
$J^{\pi}=3/2^{-}$
Ex=2.429
$J^{\pi}=5/2^{-}$
Ratio
$\theta_{c.m.}$ (degrees)

Fig. 7

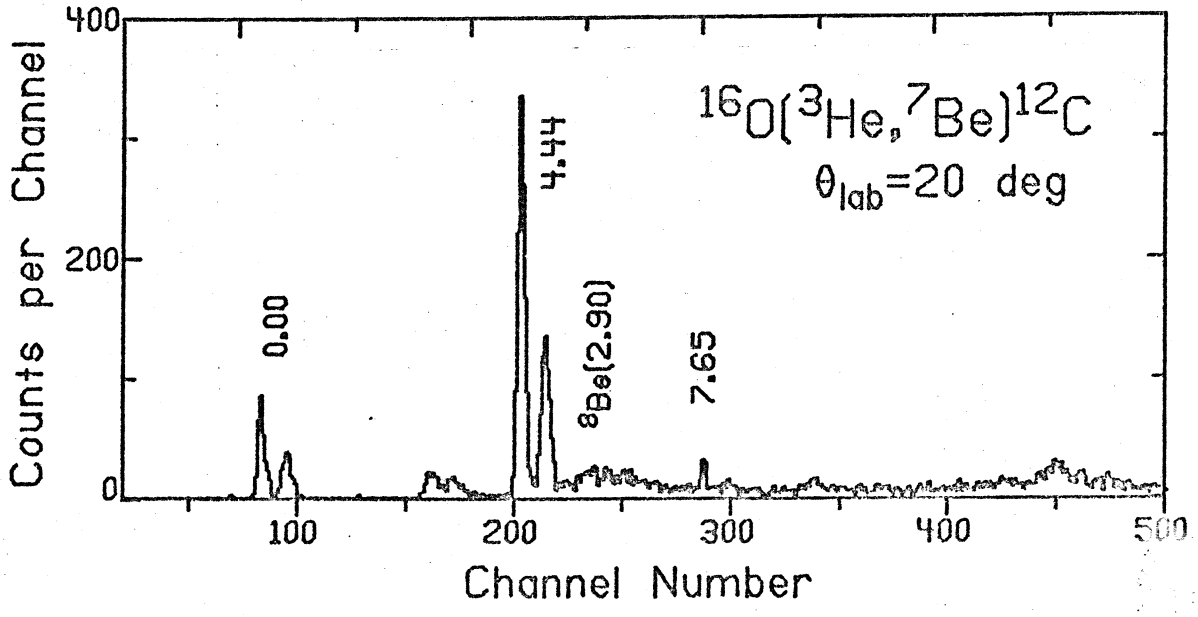
$^{16}O(^{3}He,^{7}Be)^{12}C$
$\theta_{lab}=20$ deg
Counts per Channel
Channel Number
0.00
4.44
$^{8}Be(2.90)$
7.65

Fig. 8

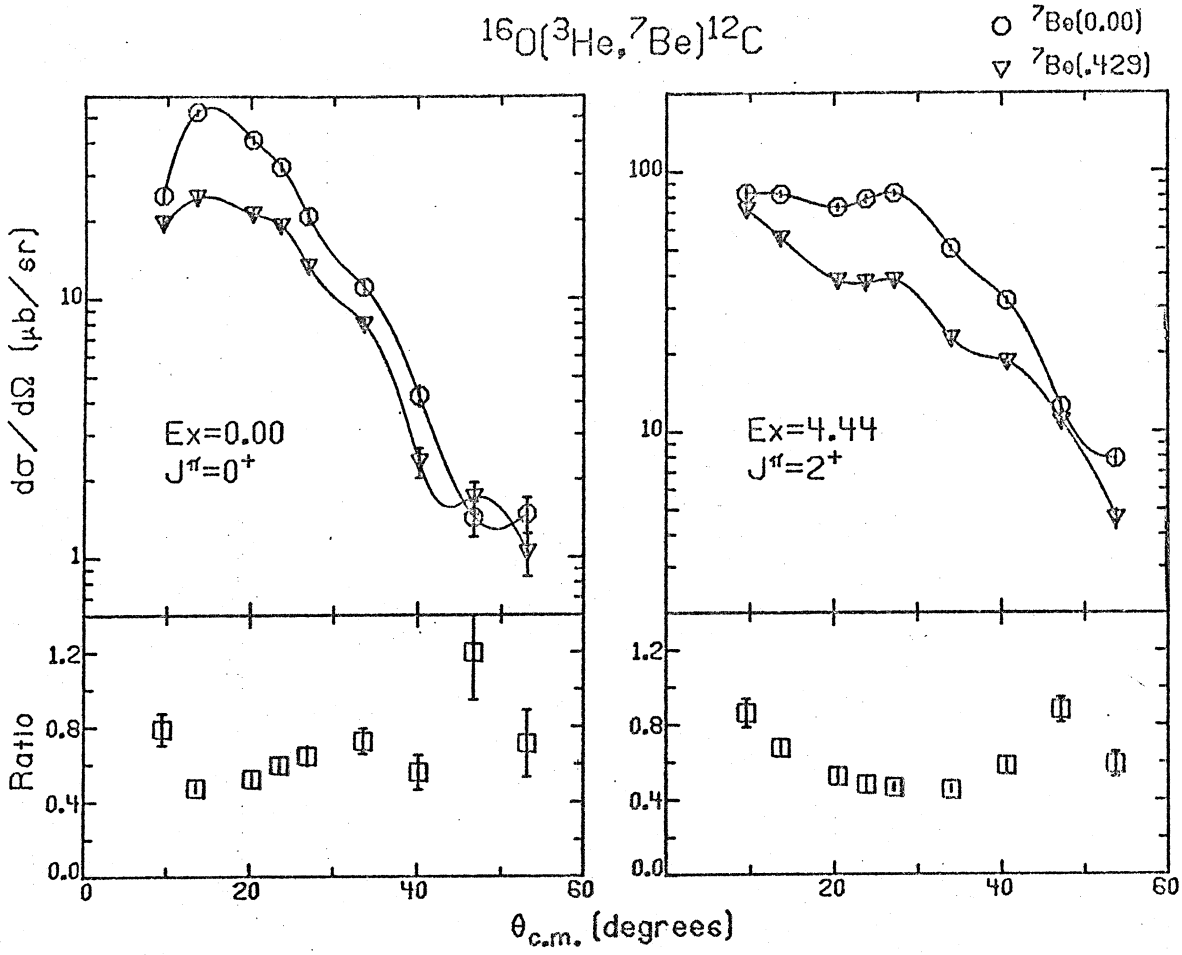
$^{16}O(^{3}He,^{7}Be)^{12}C$
○ $^{7}Be(0.00)$
▽ $^{7}Be(.429)$
dσ/dΩ (μb/sr)
Ex=0.00
$J^{\pi}=0^{+}$
Ex=4.44
$J^{\pi}=2^{+}$
Ratio
$\theta_{c.m.}$ (degrees)

Fig. 9

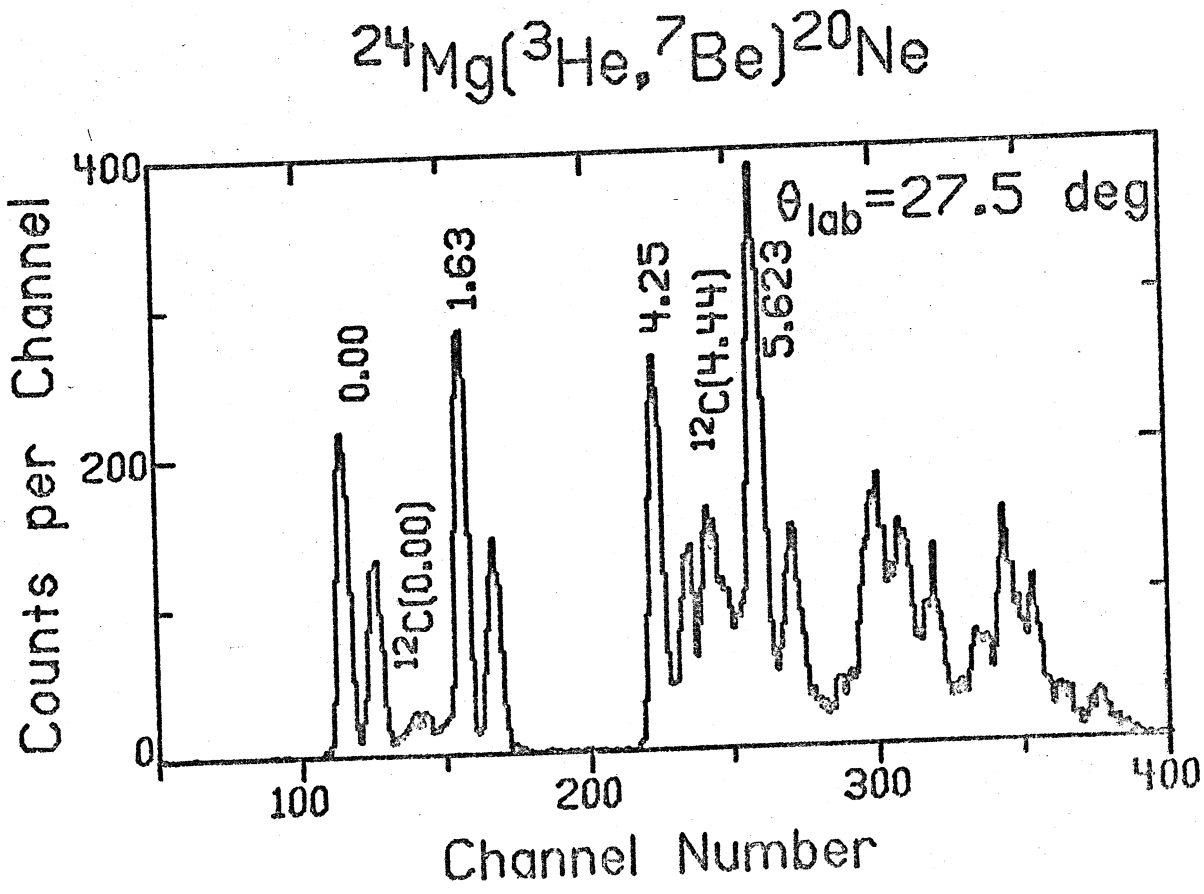
$^{24}Mg(^{3}He,^{7}Be)^{20}Ne$
θ_{lab}=27.5 deg
Counts per Channel
Channel Number
0.00
1.63
4.25
$^{12}C(4.44)$
5.623
$^{12}C(0.00)$

Fig. 10

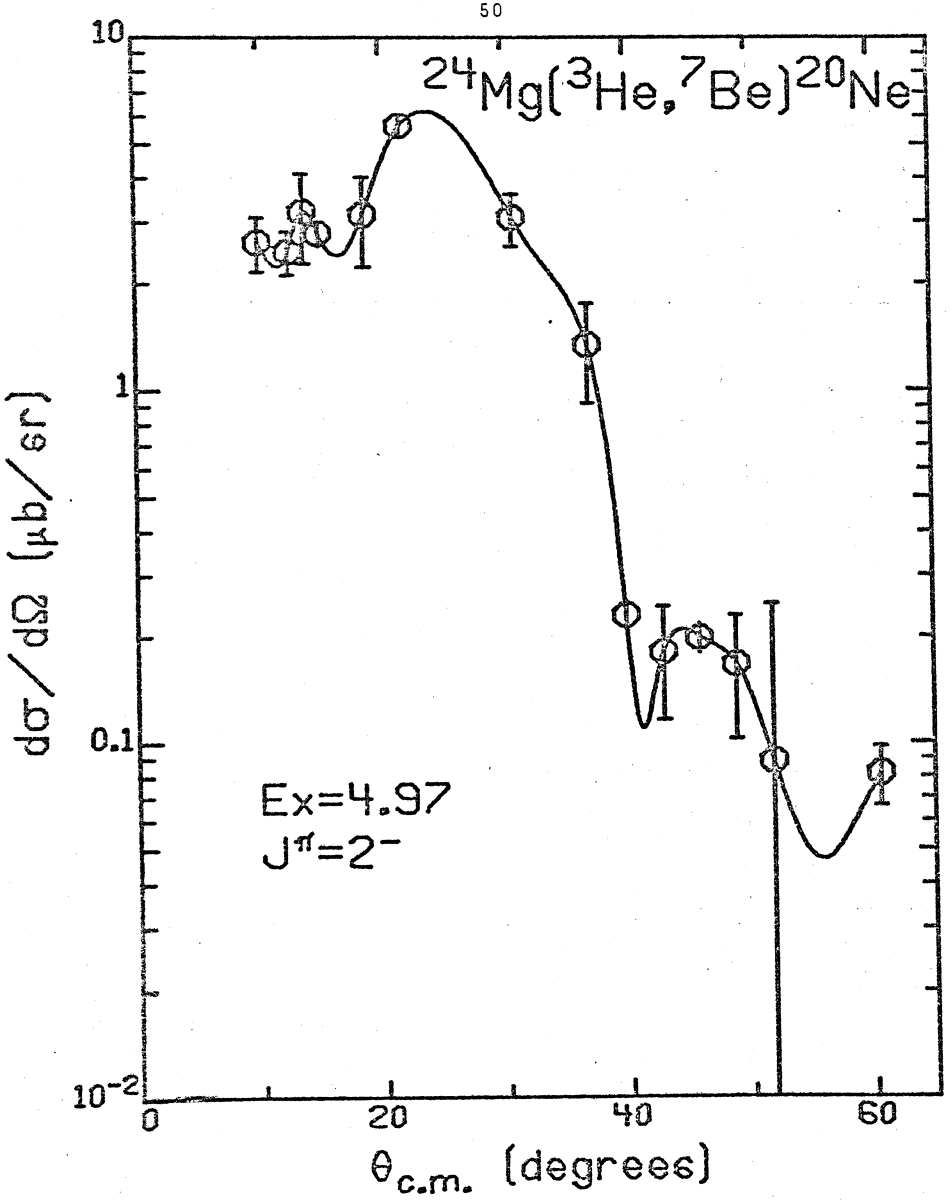
^{24}Mg(^{3}He,^{7}Be)^{20}Ne
Ex=4.97
$J^{\pi}=2^-$
dσ/dΩ (μb/sr)
$\theta_{c.m.}$ (degrees)

Fig. 11

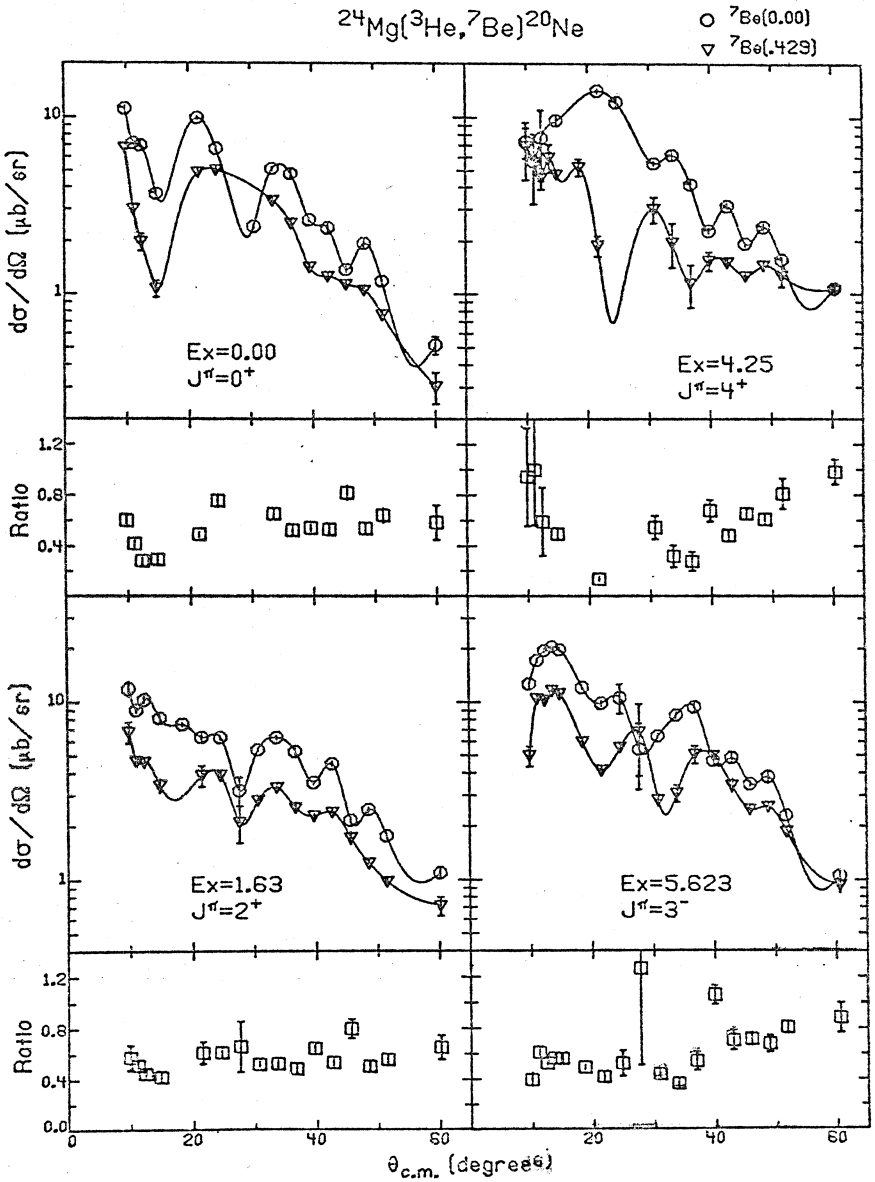
^{24}Mg(^{3}He,^{7}Be)^{20}Ne
^{7}Be(0.00)
^{7}Be(.429)
Ex=0.00
$J^{\pi}=0^+$
Ex=4.25
$J^{\pi}=4^+$
Ex=1.63
$J^{\pi}=2^+$
Ex=5.623
$J^{\pi}=3^-$
dσ/dΩ (μb/sr)
Ratio
$\theta_{c.m.}$ (degrees)

Fig. 12

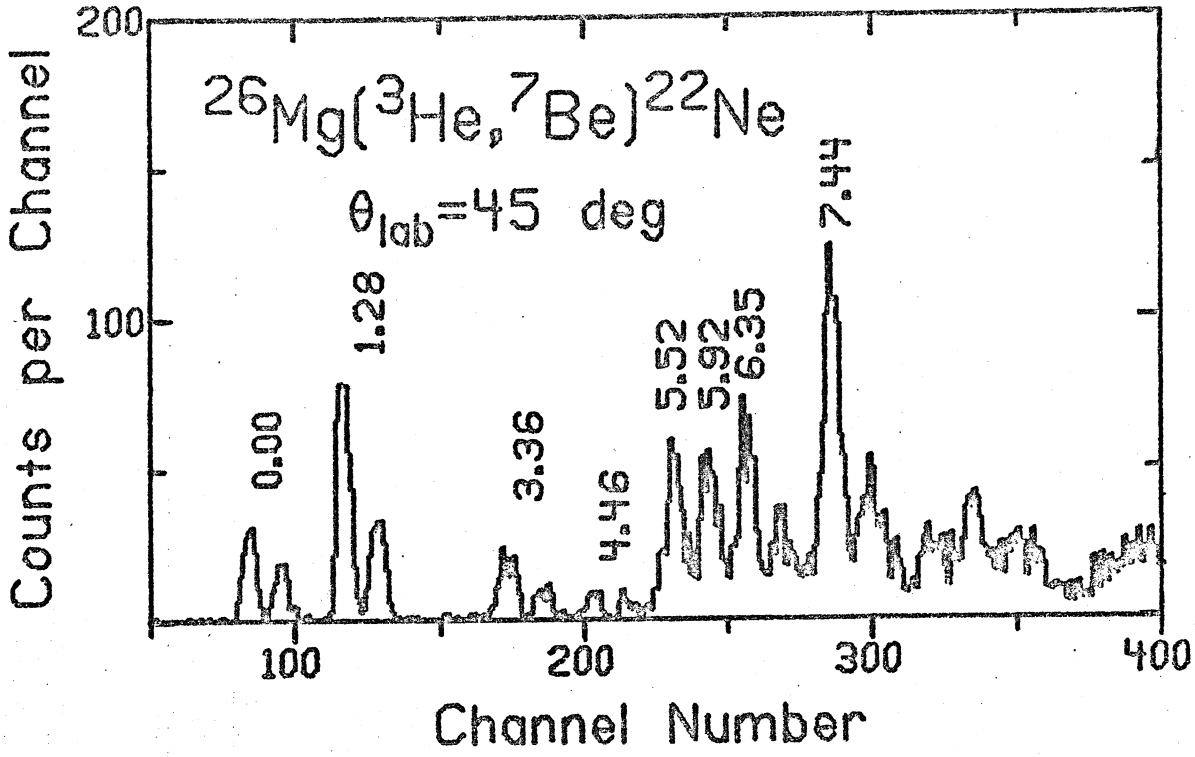
$^{26}Mg(^{3}He,^{7}Be)^{22}Ne$
θ_{lab}=45 deg
Counts per Channel
Channel Number
0.00
1.28
3.36
4.46
5.52
5.92
6.35
7.44
100
200
300
400

Fig. 13

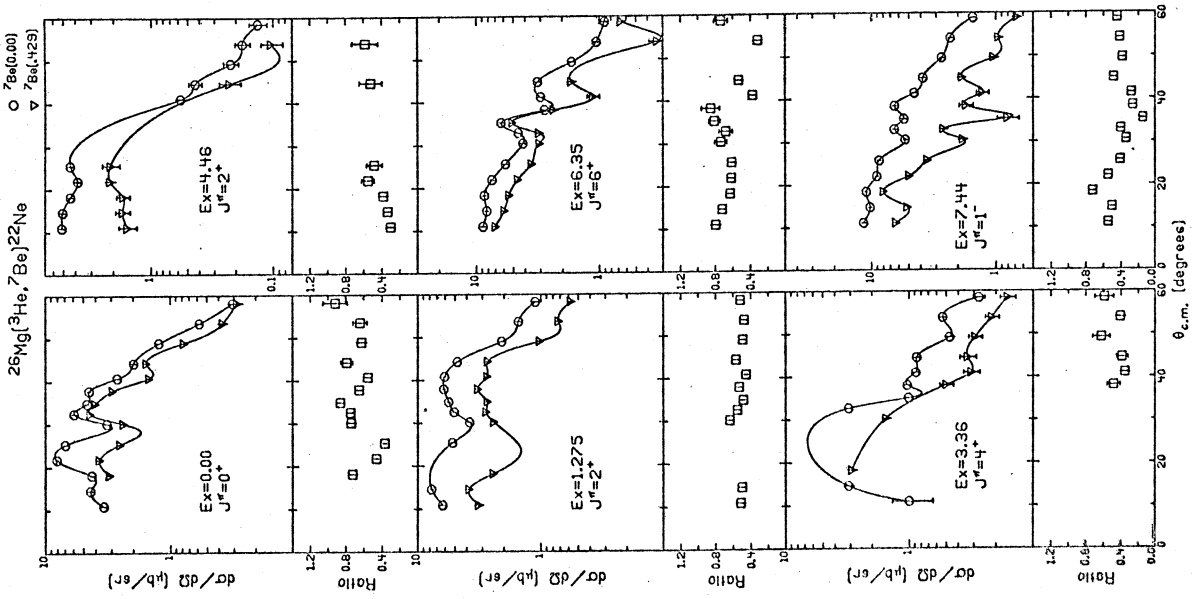
$^{26}Mg(^{3}He,^{7}Be)^{22}Ne$
○ $^{7}Be(0.00)$
▽ $^{7}Be(.429)$
Ex=0.00 $J^{\pi}=0^{+}$
Ex=1.275 $J^{\pi}=2^{+}$
Ex=3.36 $J^{\pi}=4^{+}$
Ex=4.46 $J^{\pi}=2^{+}$
Ex=6.35 $J^{\pi}=6^{+}$
Ex=7.44 $J^{\pi}=1^{-}$
dσ/dΩ (μb/sr)
Ratio
$\theta_{c.m.}$ (degrees)

Fig. 14

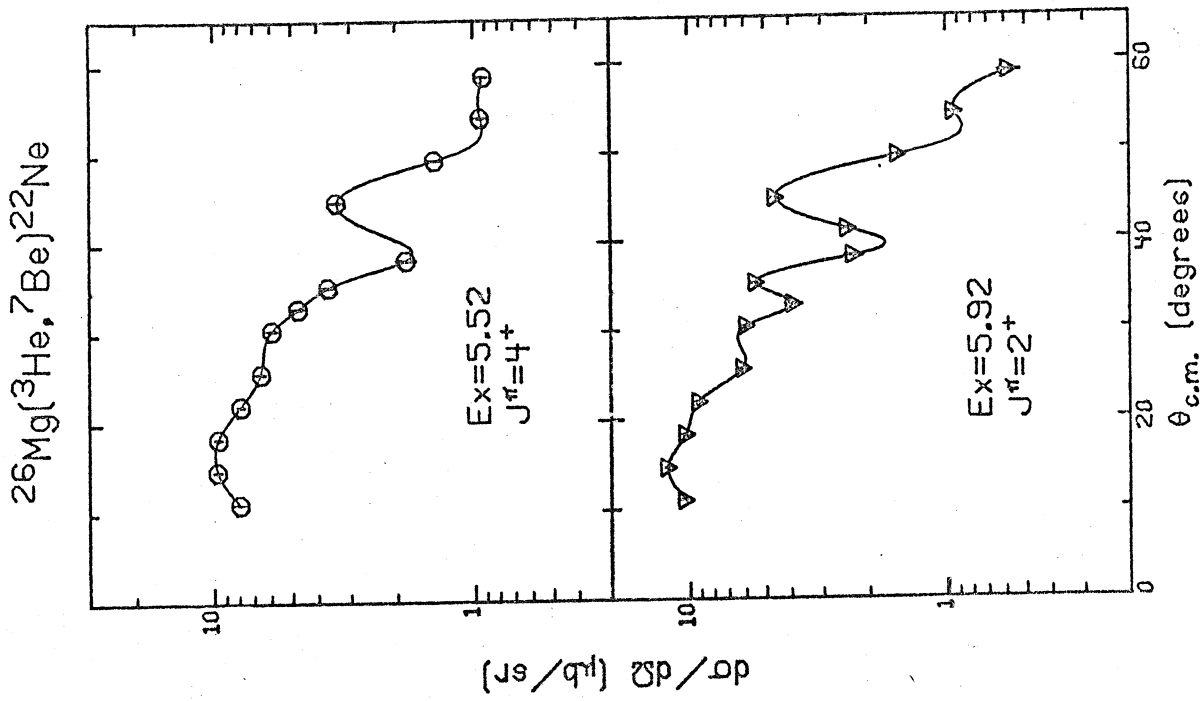
$^{26}Mg(^{3}He,^{7}Be)^{22}Ne$
Ex=5.52
$J^{\pi}=4^{+}$
Ex=5.92
$J^{\pi}=2^{+}$
$d\sigma/d\Omega$ (μb/sr)
$\theta_{c.m.}$ (degrees)

Fig. 16

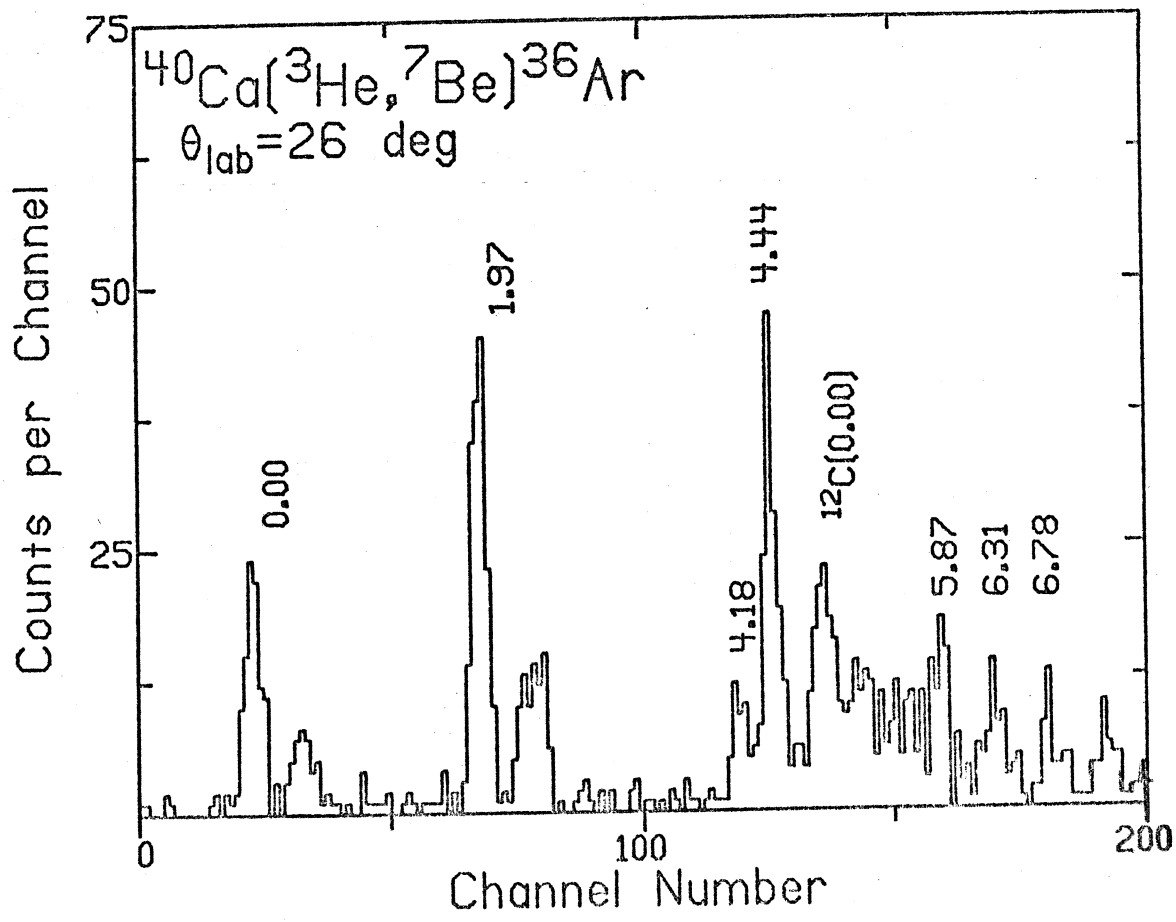
$^{40}Ca(^{3}He,^{7}Be)^{36}Ar$
θ_{lab}=26 deg
Counts per Channel
Channel Number
0.00
1.97
4.44
4.18
$^{12}C(0.00)$
5.87
6.31
6.78

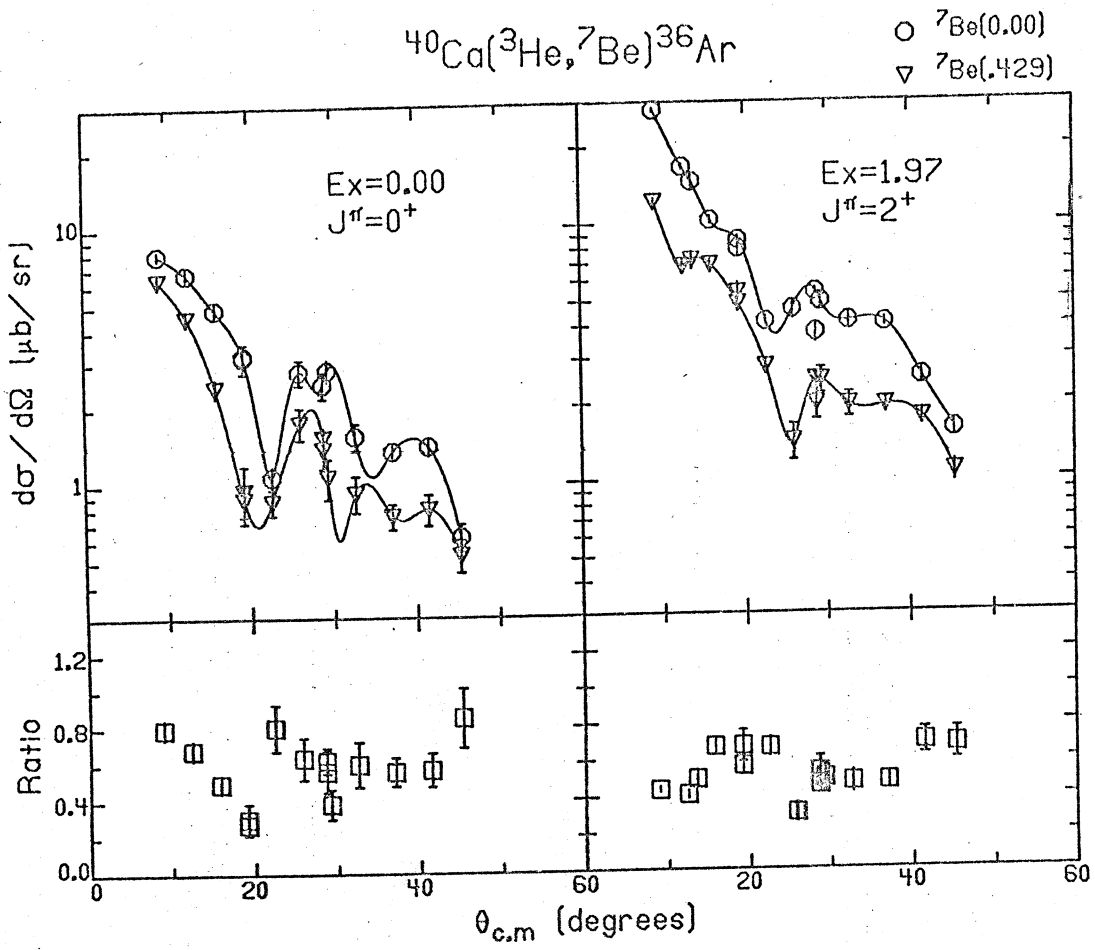
$^{40}Ca(^{3}He,^{7}Be)^{36}Ar$
○ $^{7}Be(0.00)$
▽ $^{7}Be(.429)$
Ex=0.00
$J^{\pi}=0^{+}$
Ex=1.97
$J^{\pi}=2^{+}$
dσ/dΩ (μb/sr)
Ratio
$\theta_{c.m}$ (degrees)

Fig. 17

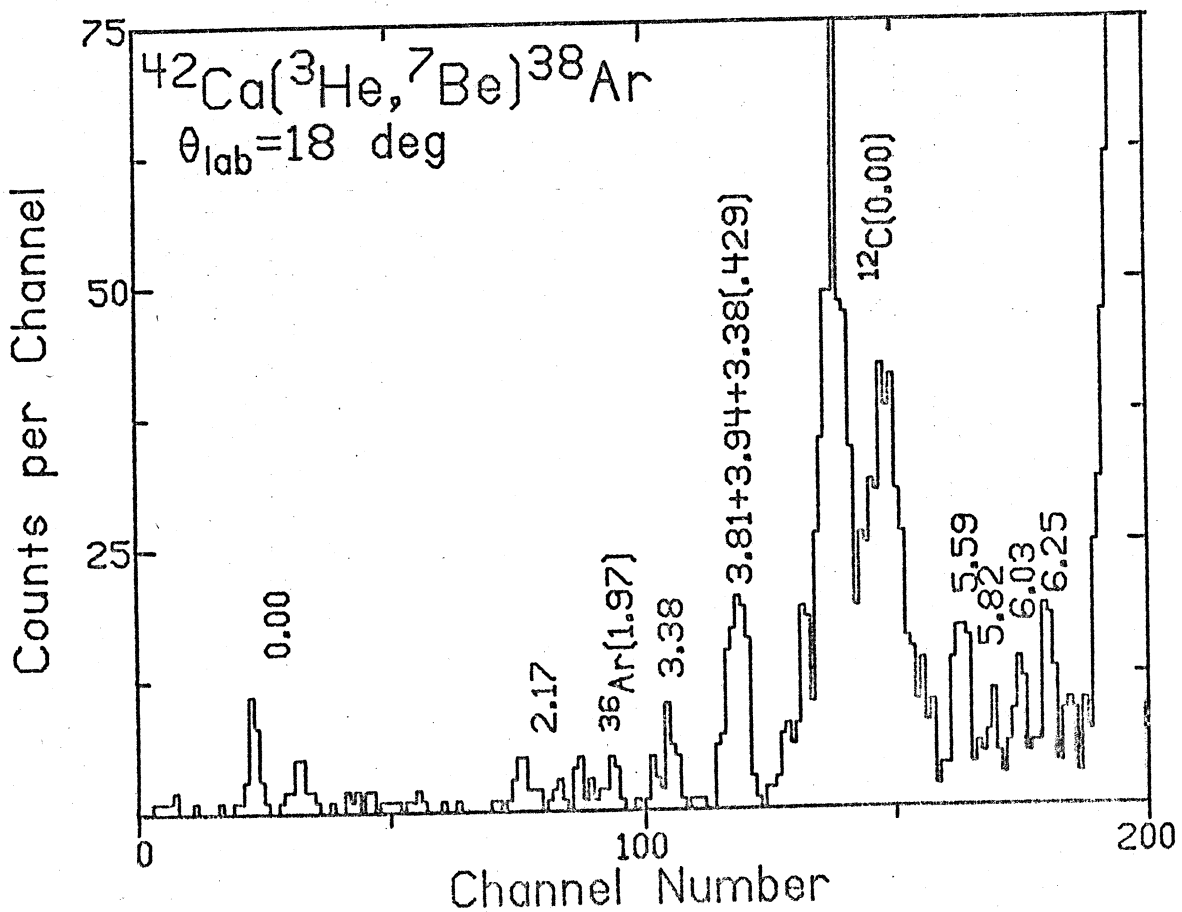
$^{42}Ca(^{3}He,^{7}Be)^{38}Ar$
θ_{lab}=18 deg
Counts per Channel
Channel Number
0.00
2.17
$^{36}Ar(1.97)$
3.38
3.81+3.94+3.38(.429)
$^{12}C(0.00)$
5.59
5.82
6.03
6.25

Fig. 18

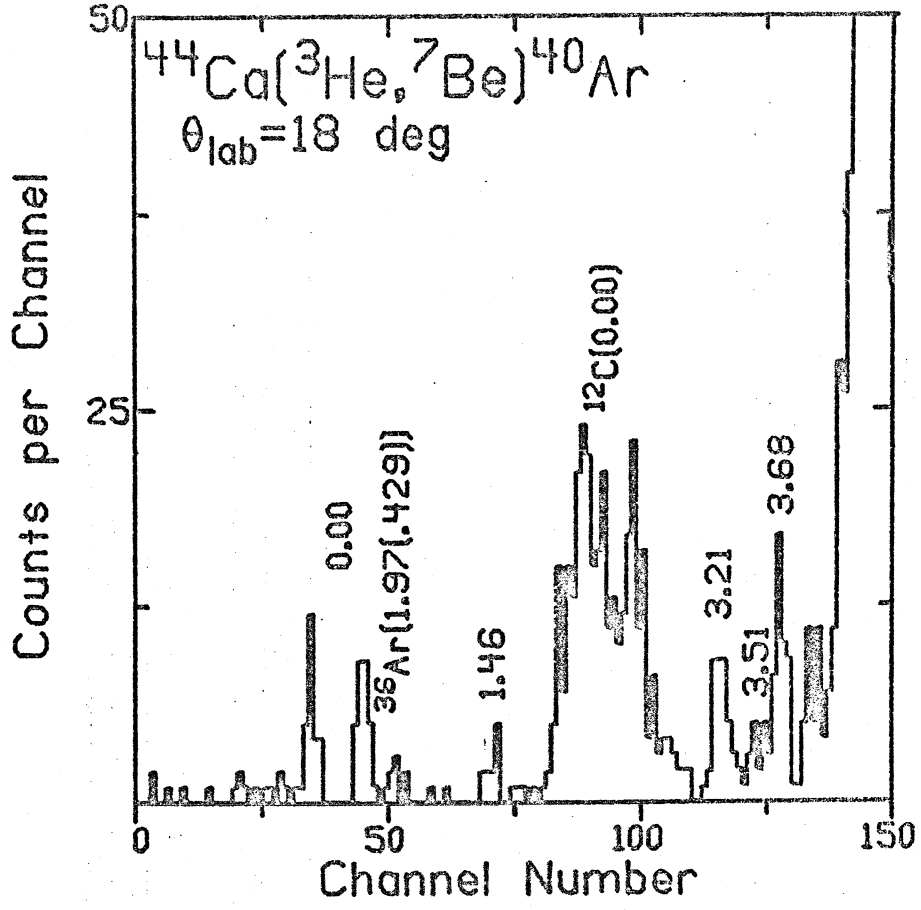
$^{44}Ca(^{3}He,^{7}Be)^{40}Ar$
θ_{lab}=18 deg
Counts per Channel
Channel Number
0.00
^{36}Ar(1.97[.429])
1.46
^{12}C(0.00)
3.21
3.51
3.68
0
50
100
150
25
50

Fig. 19

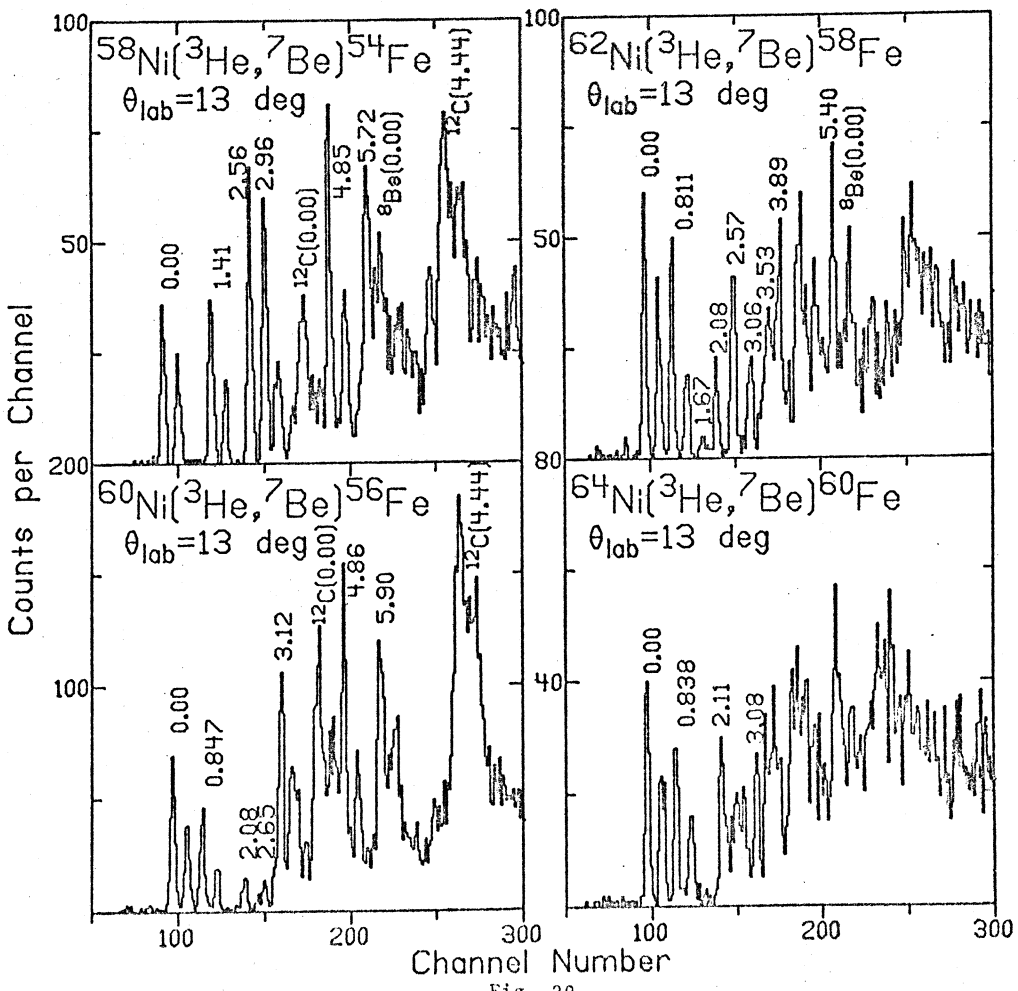
$^{58}Ni(^{3}He,^{7}Be)^{54}Fe$
θ_{lab}=13 deg
0.00
1.41
2.56
2.96
^{12}C(0.00)
4.85
5.72
^{8}Be(0.00)
^{12}C(4.44)
$^{62}Ni(^{3}He,^{7}Be)^{58}Fe$
θ_{lab}=13 deg
0.00
0.811
1.67
2.08
2.57
3.06
3.53
3.89
5.40
^{8}Be(0.00)
$^{60}Ni(^{3}He,^{7}Be)^{56}Fe$
θ_{lab}=13 deg
0.00
0.847
2.08
2.65
3.12
^{12}C(0.00)
4.86
5.90
^{12}C(4.44)
$^{64}Ni(^{3}He,^{7}Be)^{60}Fe$
θ_{lab}=13 deg
0.00
0.838
2.11
3.08
Counts per Channel
Channel Number
100
200
300
50
80
40

Fig. 20

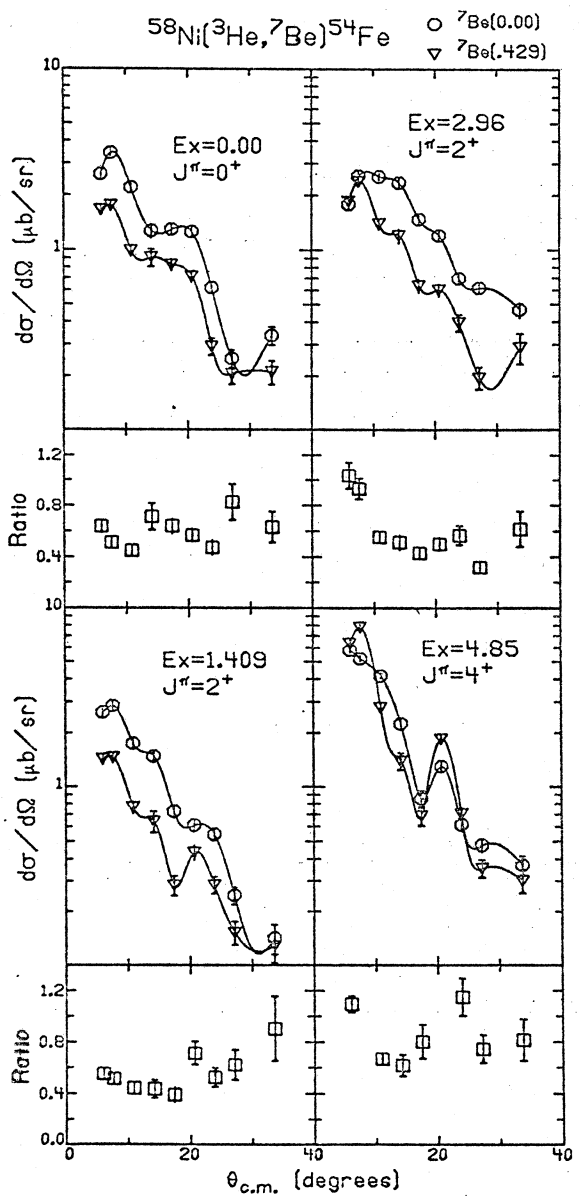
58Ni(3He,7Be)54Fe
○ 7Be(0.00)
▽ 7Be(.429)
Ex=0.00
Jπ=0+
Ex=2.96
Jπ=2+
Ex=1.409
Jπ=2+
Ex=4.85
Jπ=4+
dσ/dΩ (μb/sr)
Ratio
θc.m. (degrees)

Fig. 21

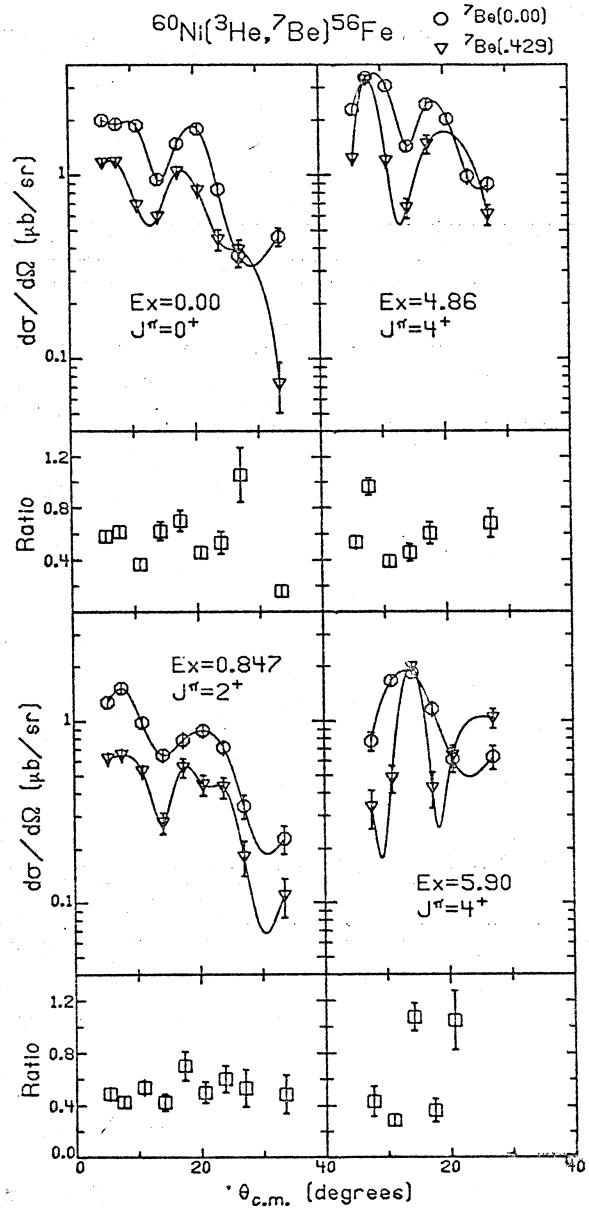
60Ni(3He,7Be)56Fe
○ 7Be(0.00)
▽ 7Be(.429)
Ex=0.00
Jπ=0+
Ex=4.86
Jπ=4+
Ex=0.847
Jπ=2+
Ex=5.90
Jπ=4+
dσ/dΩ (μb/sr)
Ratio
θc.m. (degrees)

Fig. 22

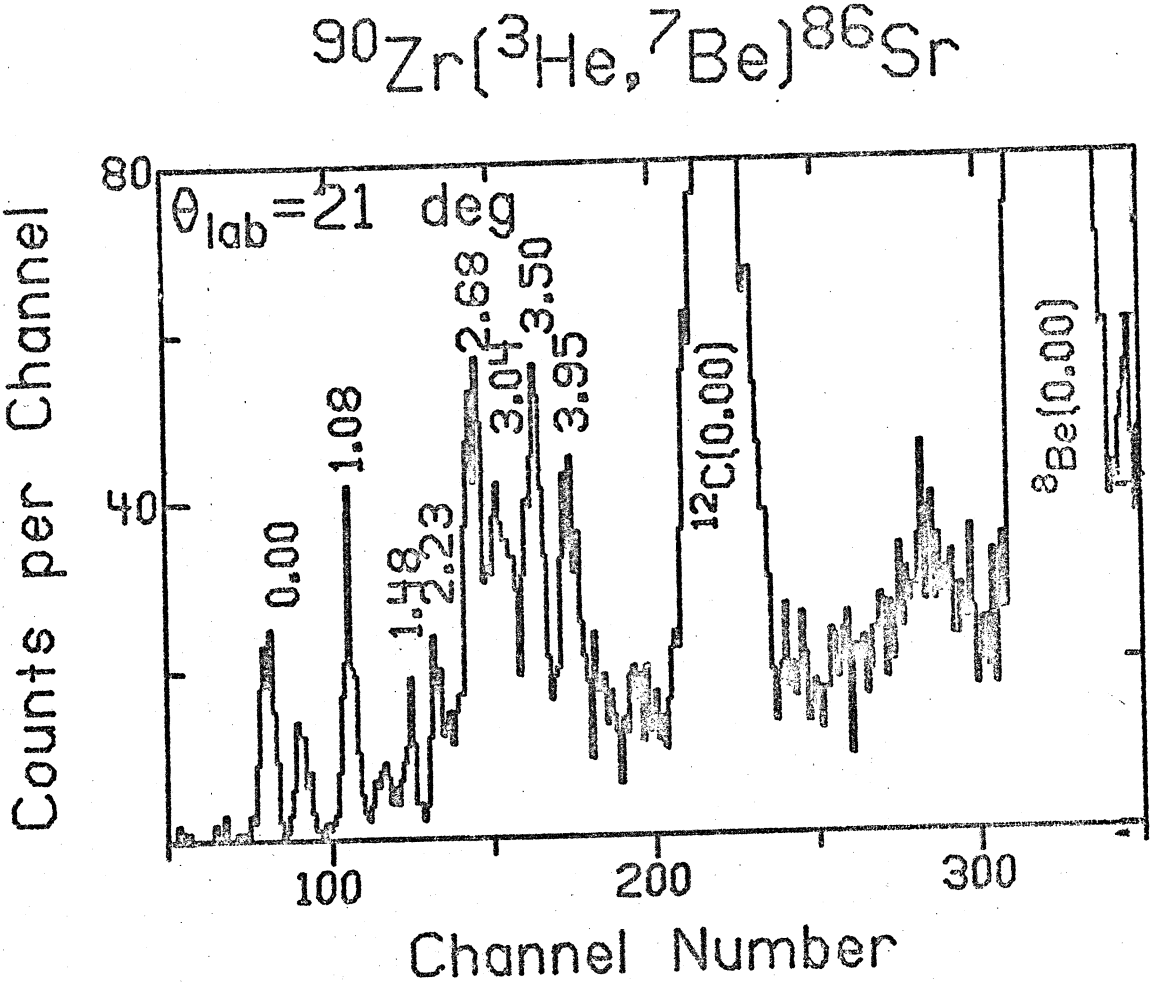
$^{90}Zr(^{3}He,^{7}Be)^{86}Sr$
θ_{lab}=21 deg
Counts per Channel
Channel Number
0.00
1.08
1.48
2.23
2.68
3.04
3.50
3.95
^{12}C(0.00)
^{8}Be(0.00)
80
40
100
200
300

Fig. 23

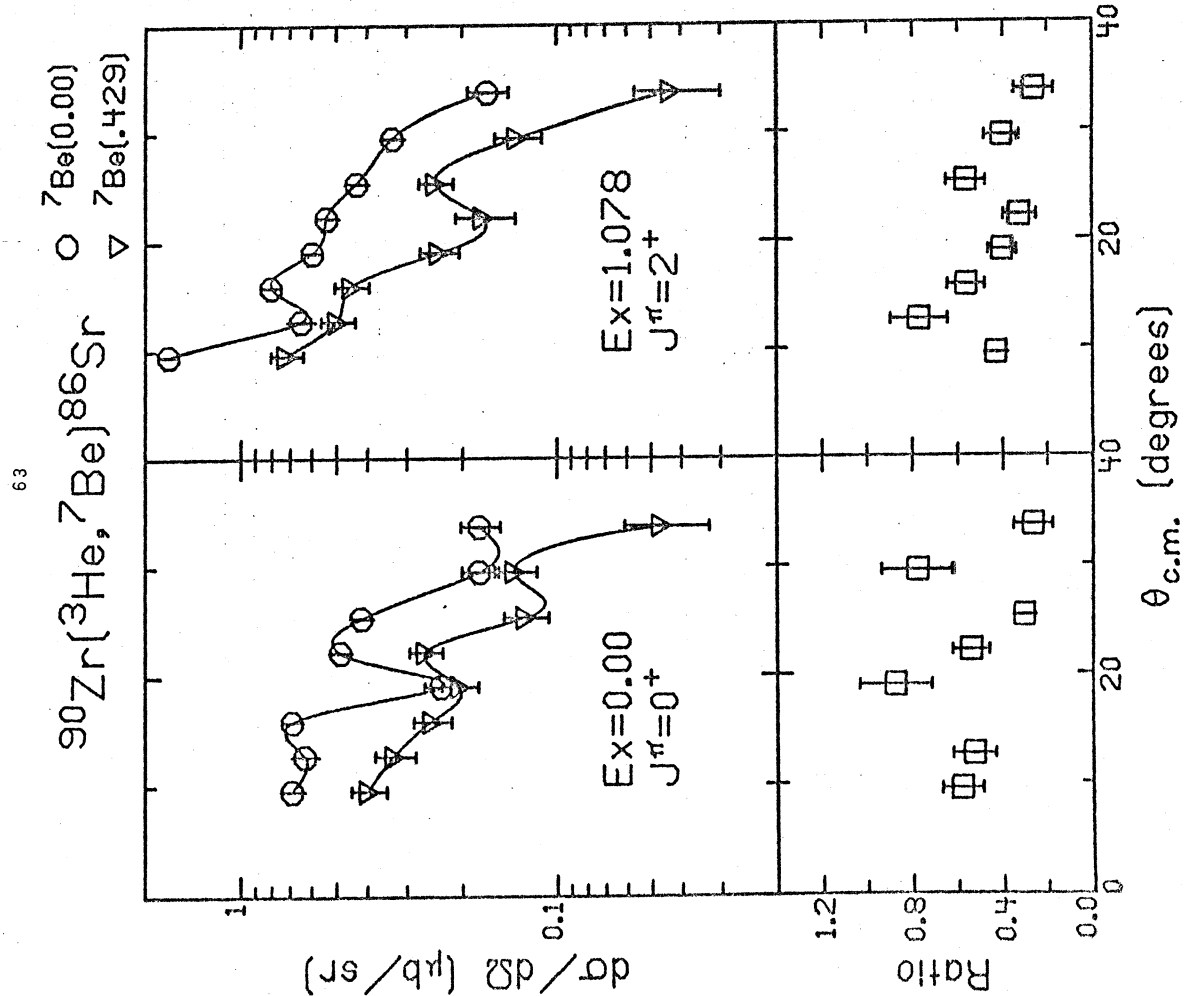
$^{90}Zr(^{3}He,^{7}Be)^{86}Sr$
○ ^{7}Be(0.00)
▽ ^{7}Be(.429)
Ex=1.078
$J^{\pi}=2^{+}$
Ex=0.00
$J^{\pi}=0^{+}$
$d\sigma/d\Omega$ (μb/sr)
Ratio
$\theta_{c.m.}$ (degrees)
1
0.1
1.2
0.8
0.4
0.0
40
20
0

Fig. 24

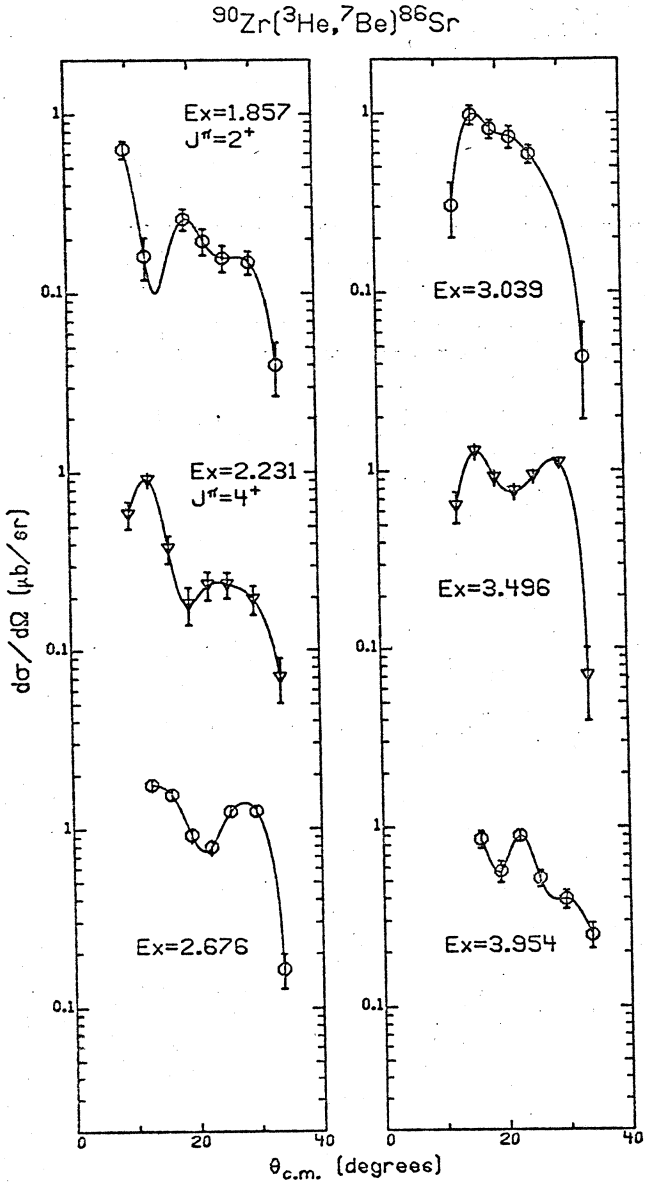
$^{90}Zr(^{3}He,^{7}Be)^{86}Sr$
Ex=1.857
$J^{\pi}=2^{+}$
Ex=2.231
$J^{\pi}=4^{+}$
Ex=2.676
Ex=3.039
Ex=3.496
Ex=3.954
$d\sigma/d\Omega$ (μb/sr)
$\theta_{c.m.}$ (degrees)

Fig. 25

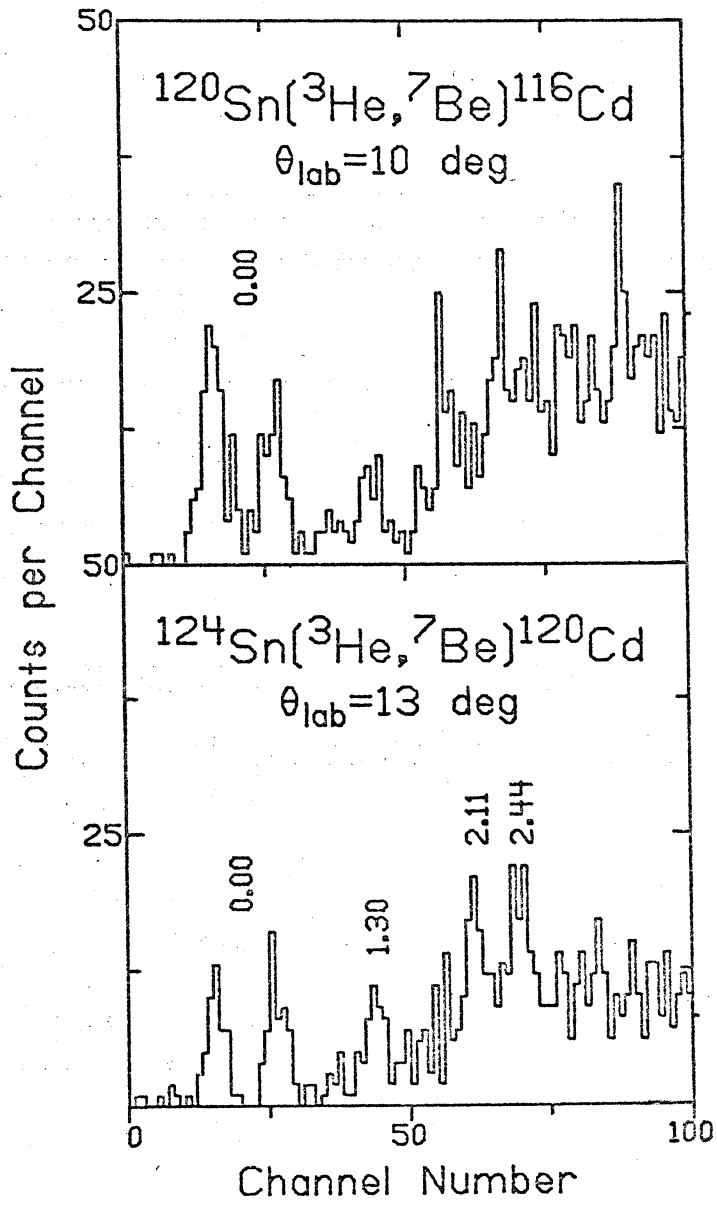
$^{120}Sn(^{3}He,^{7}Be)^{116}Cd$
θ_{lab}=10 deg
0.00
$^{124}Sn(^{3}He,^{7}Be)^{120}Cd$
θ_{lab}=13 deg
0.00
1.30
2.11
2.44
Counts per Channel
Channel Number

Fig. 26

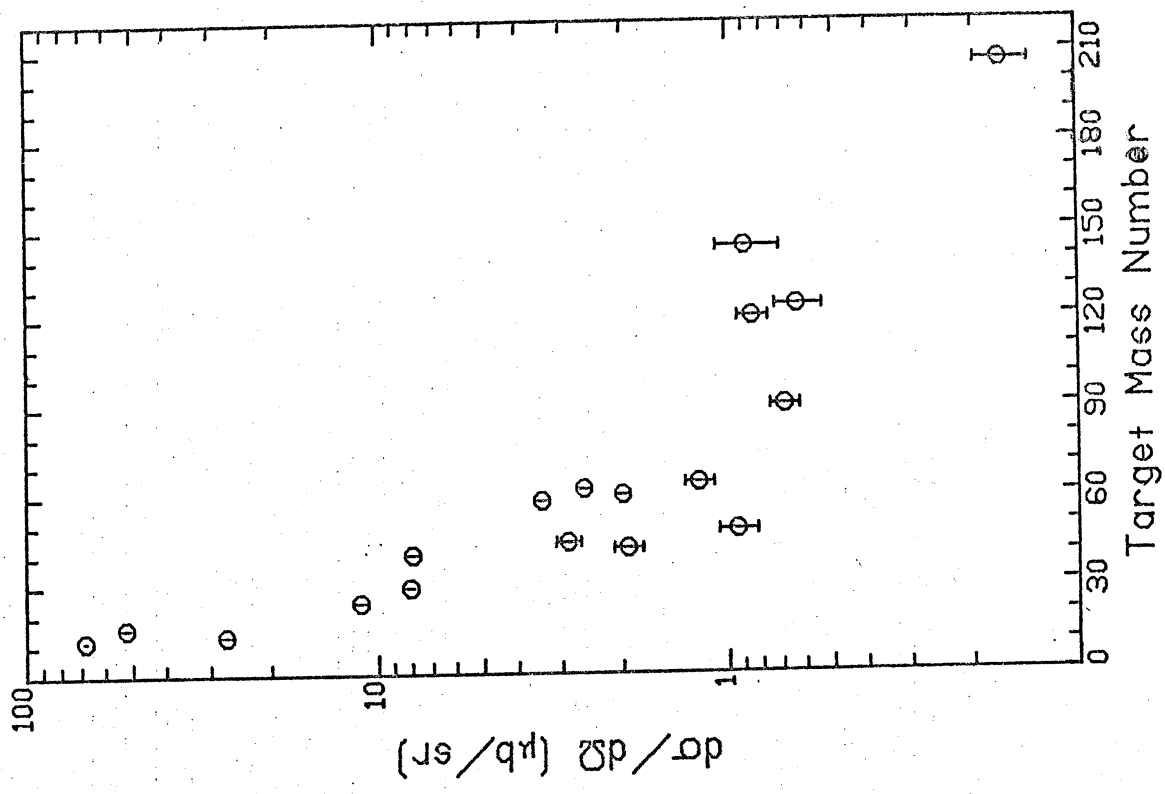
dσ/dΩ (μb/sr)
100
10
1
0
30
60
90
120
150
180
210
Target Mass Number

Fig. 27

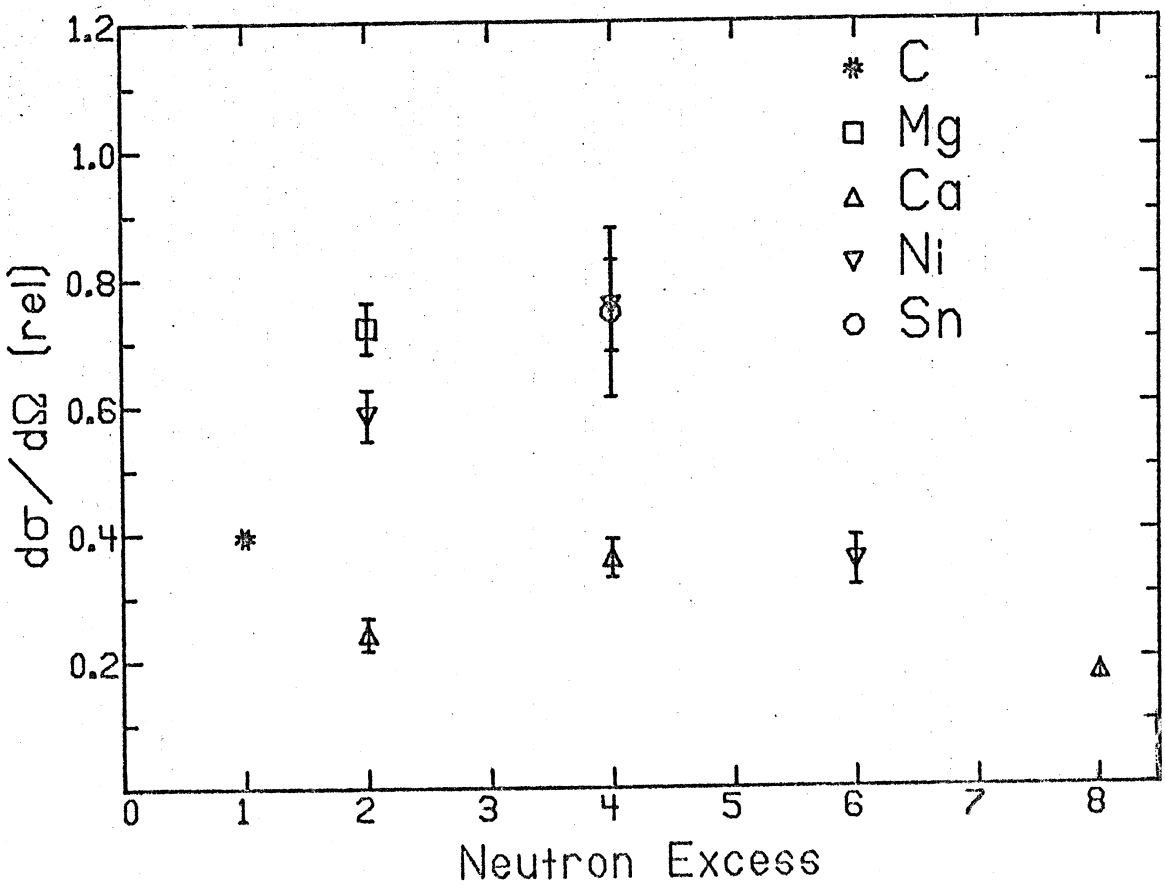
dσ/dΩ (rel)
1.2
1.0
0.8
0.6
0.4
0.2
0
1
2
3
4
5
6
7
8
Neutron Excess
C
Mg
Ca
Ni
Sn

Fig. 28

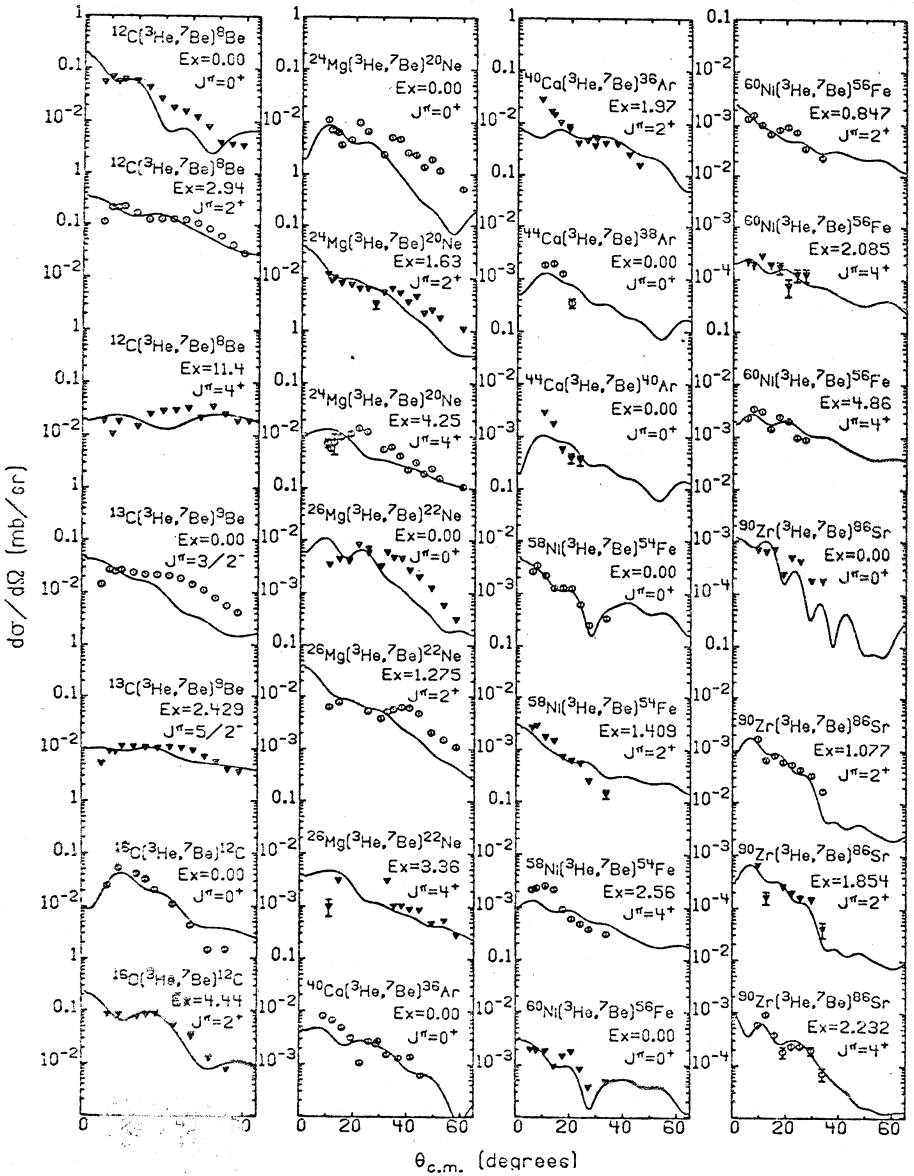
12C(3He,7Be)8Be Ex=0.00 Jπ=0+
12C(3He,7Be)8Be Ex=2.94 Jπ=2+
12C(3He,7Be)8Be Ex=11.4 Jπ=4+
13C(3He,7Be)9Be Ex=0.00 Jπ=3/2-
13C(3He,7Be)9Be Ex=2.429 Jπ=5/2-
16O(3He,7Be)12C Ex=0.00 Jπ=0+
16O(3He,7Be)12C Ex=4.44 Jπ=2+
24Mg(3He,7Be)20Ne Ex=0.00 Jπ=0+
24Mg(3He,7Be)20Ne Ex=1.63 Jπ=2+
24Mg(3He,7Be)20Ne Ex=4.25 Jπ=4+
26Mg(3He,7Be)22Ne Ex=0.00 Jπ=0+
26Mg(3He,7Be)22Ne Ex=1.275 Jπ=2+
26Mg(3He,7Be)22Ne Ex=3.36 Jπ=4+
40Ca(3He,7Be)36Ar Ex=0.00 Jπ=0+
40Ca(3He,7Be)36Ar Ex=1.97 Jπ=2+
44Ca(3He,7Be)38Ar Ex=0.00 Jπ=0+
44Ca(3He,7Be)40Ar Ex=0.00 Jπ=0+
58Ni(3He,7Be)54Fe Ex=0.00 Jπ=0+
58Ni(3He,7Be)54Fe Ex=1.409 Jπ=2+
58Ni(3He,7Be)54Fe Ex=2.56 Jπ=4+
60Ni(3He,7Be)56Fe Ex=0.00 Jπ=0+
60Ni(3He,7Be)56Fe Ex=0.847 Jπ=2+
60Ni(3He,7Be)56Fe Ex=2.085 Jπ=4+
60Ni(3He,7Be)56Fe Ex=4.86 Jπ=4+
90Zr(3He,7Be)86Sr Ex=0.00 Jπ=0+
90Zr(3He,7Be)86Sr Ex=1.077 Jπ=2+
90Zr(3He,7Be)86Sr Ex=1.854 Jπ=2+
90Zr(3He,7Be)86Sr Ex=2.232 Jπ=4+
dσ/dΩ (mb/sr)
θc.m. (degrees)

Fig. 29

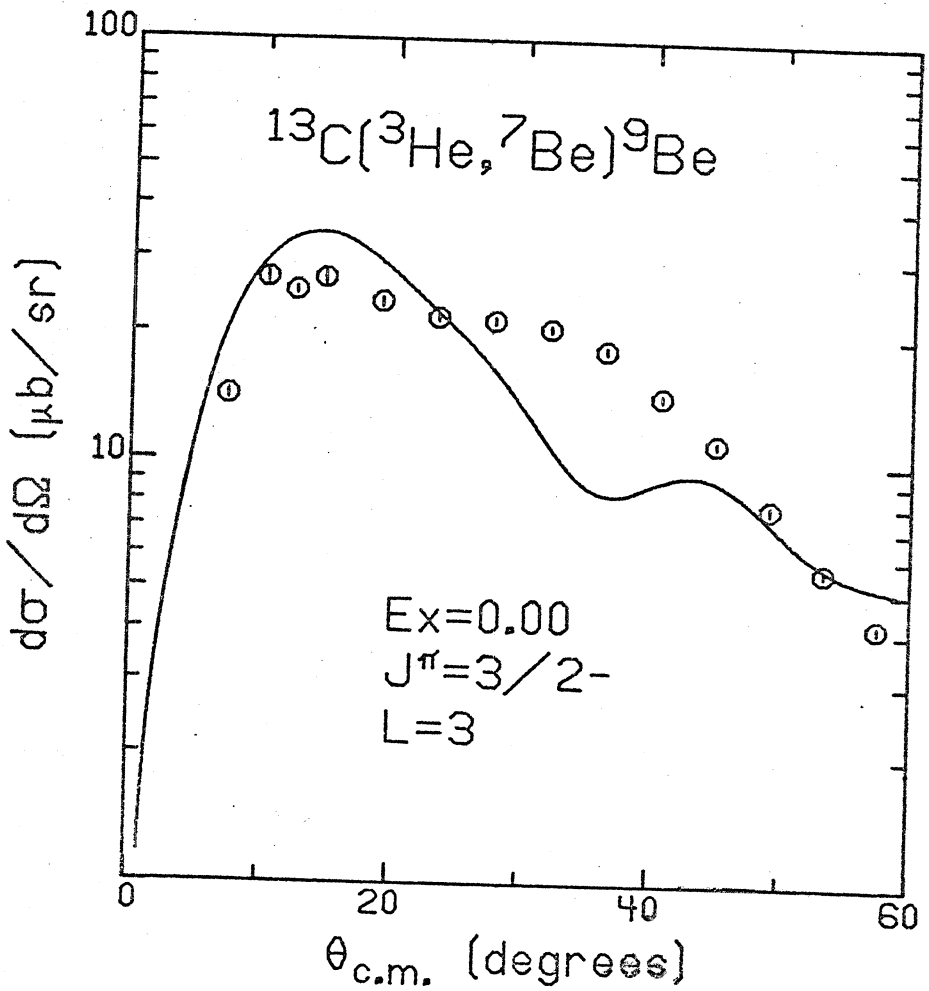
13C(3He,7Be)9Be
Ex=0.00
Jπ=3/2-
L=3
dσ/dΩ (μb/sr)
θc.m. (degrees)

Fig. 30